

REVIEW

Open Access



Thermochromic phantoms and paint to characterize and model image-guided thermal ablation and ablation devices: a review

Ayele H. Negussie^{1*}, Robert Morhard¹, Jocelyne Rivera¹, Jose F. Delgado^{1,2}, Sheng Xu¹ and Bradford J. Wood^{1,2}

Abstract

Heat-based local ablation techniques are effective treatments for specific oligometastatic and localized cancers and are being studied for their potential to induce immunogenic cell death and augment systemic immune responses to immunotherapies. The diverse technologies associated with thermal therapy have an unmet need for method development to enable device-specific experimentation, optimization, calibration and refinement of the parameter space to optimize therapeutic intent while minimizing side effects or risk to the patient. Quality assurance, training, or comparing thermal dose among different modalities or techniques using animal models is time and resource intensive. Therefore, the application and use of tissue mimicking thermosensitive, thermochromic liquid crystal and thermochromic paint phantom models may reduce costs and hurdles associated with animal use. Further, their homogenous composition may enable more precise assessment of ablative techniques. This review utilized SciFinder, Web of Science, PubMed and EMBASE to systematically evaluate the literature describing the background and applications of thermochromic liquid crystal, thermochromic paint and tissue-mimicking thermochromic phantoms used to characterize the thermal effects of ablation devices with a focus on facilitating their use across the medical device development life cycle.

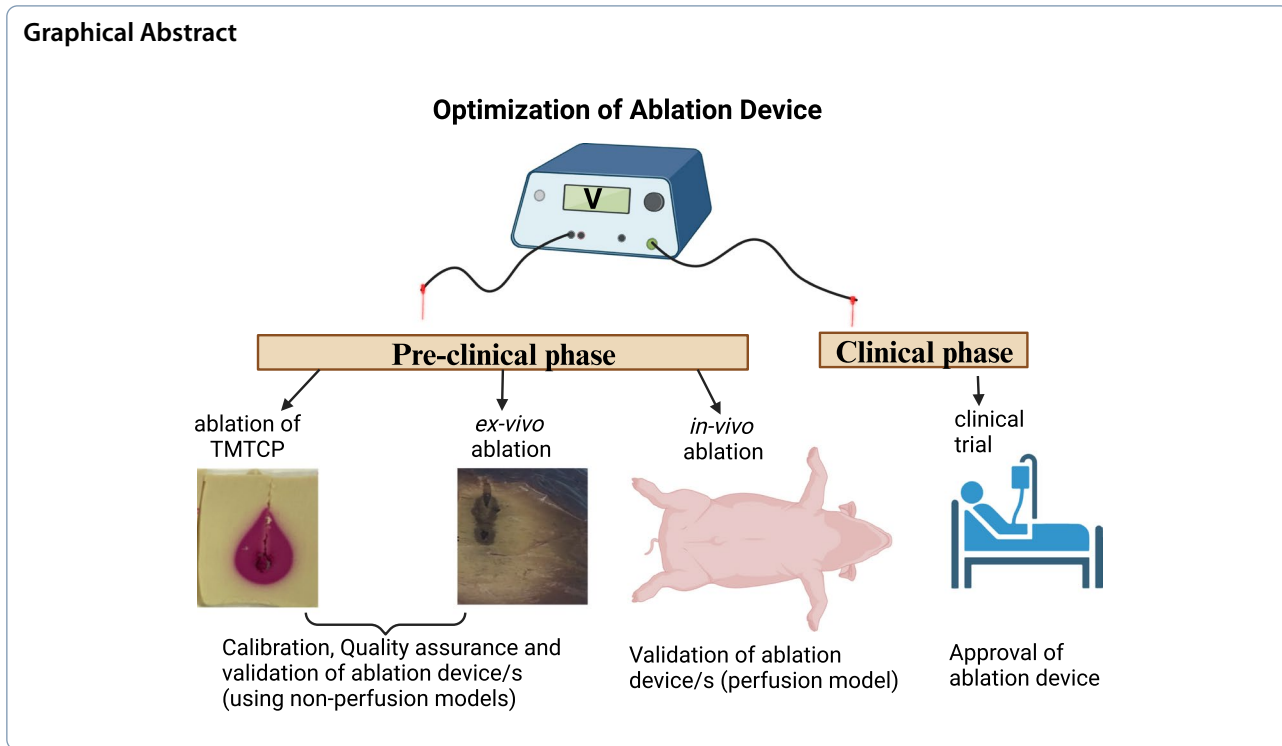
*Correspondence:

Ayele H. Negussie
negussiea@nih.gov

Full list of author information is available at the end of the article



This is a U.S. Government work and not under copyright protection in the US; foreign copyright protection may apply 2024, corrected publication 2024. **Open Access** This article is licensed under a Creative Commons Attribution 4.0 International License, which permits use, sharing, adaptation, distribution and reproduction in any medium or format, as long as you give appropriate credit to the original author(s) and the source, provide a link to the Creative Commons licence, and indicate if changes were made. The images or other third party material in this article are included in the article's Creative Commons licence, unless indicated otherwise in a credit line to the material. If material is not included in the article's Creative Commons licence and your intended use is not permitted by statutory regulation or exceeds the permitted use, you will need to obtain permission directly from the copyright holder. To view a copy of this licence, visit <http://creativecommons.org/licenses/by/4.0/>.



Introduction

Hyperthermia and thermal ablation devices deposit electromagnetic energy locally to heat tissue and treat localized diseases, such as cancer, under image guidance [1]. During the last several decades, thermal ablation (TA) devices have emerged as important surgical, laparoscopic, percutaneous and minimally-invasive hyperthermia treatment modalities for cancer [2]. TA is a clinical procedure that delivers therapeutic energy (target temperature >60 °C) into soft or bone tissues with the goal of eradicating small lesions in lung, kidney, liver, bone and other tissues, either as a mono-therapy or in combination with other treatment modalities (surgery, chemotherapy, radiation, immunotherapy, or trans-arterial chemoembolization or radioembolization) [3–9] with minimal off-target thermal damage to surrounding healthy tissue. Irreversible tissue damage from temperature effects depends on temperature and duration of thermal application [10], in an Arrhenius-like non-linear relationship between temperature and duration. The traditional Arrhenius model has been used for many decades to describe protein denaturation and cell death processes [11, 12]. This temperature-dependent rate constant (Arrhenius equation) is described by:

$$k = A \exp\left(-\frac{E_a}{RT}\right) \tag{1}$$

Where A is the “frequency factor” (s⁻¹), E_a is the energy of activation (kJ mol⁻¹), R is the gas constant and T is the absolute temperature [13]. This model established an exponential relationship between tissue exposed to elevated temperatures and cells subjected to thermal injury. For instance, for a specific temperature and time, the model’s fit parameters determine the probability of cell death or damage [13].

Another model for predicting hyperthermic injury is the thermal isoeffective dose (TID). This method (see the following equation) is based upon time-temperature relationships for complete cell killing.

$$TID \text{ (or CEM43)} = \int_0^t R^{(43-T)} dt \text{ (min)} \tag{2}$$

TID is the thermal dose in units of cumulative equivalent minutes at 43 °C (CEM43), where T represents the temperature applied to the target tissue, R is the factor to compensate for a 1 °C temperature change, and dt is the time at temperature T (°C) [14]. In principle, the TID concept is a normalizing method to convert time-temperature exposures to an equivalent exposure time in minutes at a reference temperature (commonly 43 °C) [15]. This model is widely used to explore the required duration for heating to achieve tissue thermal damage and is commonly applied to define exposure thresholds [12].

TA can potentially make cancer cells more sensitive to radiation, and certain chemo- and immunotherapeutics [16]. Therefore, TA devices are expected to deliver sufficient heat to bring desirable effects with minimal damage to normal biological tissue. TA devices also need to be calibrated and characterized for proper reproducible and standardized performance, to maintain patient safety and efficacy. Bovine serum albumin (BSA) containing polyacrylamide gel (PAG) was an early tissue mimicking phantom fabricated to visualize three-dimensional coagulation temperature distribution during radiofrequency ablation (RFA) [17]. However, this phantom does not report the achieved temperature post-RFA, as protein coagulation is visually similar at any temperature above 40°C. In addition, the achieved ablation size at a given RF power decreases as the pH of the phantom increases. For this, tissue mimicking thermochromic phantoms (TMTCP) containing thermochromic materials that change color in response to temperature alterations were developed [18–22] and increasingly used in the design, optimization, and quality assurance of thermal devices in support of intended performance [23–28], all of which may facilitate clinical translation or optimization of device and procedure.

Characterizing thermal output and tracking the temperature in the target region is useful to predict the depth and size of the ablation zone and facilitate development of ablation protocols to optimize clinical algorithms and potential clinical outcomes. These phantoms, even though they fail to capture every physiologic phenomenon (such as blood perfusion, tissue heterogeneity, polarity, and charring), they still may accurately estimate thermal dose and effects of altered parameters, and thus may play a role in preclinical testing of TA devices [21, 26].

TMTCPs can be fabricated for a wide range of needs. They can incorporate irreversible or reversible thermochromic materials. The use of reversible thermochromic materials allows for transient analysis of heat transfer, and irreversible materials have been utilized to visualize the maximum temperature distribution and estimate the resultant ablation morphology [19, 20, 29]. The techniques often involve cutting the phantom, imaging and comparing the color intensity with reference phantoms heated in a pre-calibrated water bath [18]. The signal from the image is generally quantified by either intensity or hue, defined in terms of red-green-blue (RGB) and paired with the correlative temperature that caused that specific intensity. TMTCPs can include additives to make them electrically conductive for use with RFA and IRE, or with albumin to allow for MR-enabled temperature distribution due to protein denaturation which alters the transverse relaxation time (T_2). The purpose of this review is to discuss

the spectrum of medical applications for tissue mimicking thermochromic phantoms as tissue models for characterizing and calibrating different ablation devices. Thermochromic materials whose thermochromism requires high temperatures (>200°C) or is due to interaction of ultraviolet light are excluded from this review.

Thermochromic materials

Thermochromic materials are materials which exhibit thermochromism—a unique color changing property displayed upon change in temperature [30]. They include liquid crystals [31], leuco dye [32], inorganic thermochromic materials [33], hybrids of inorganic and organic materials [34], quantum dots [35], polymers [36] or dye-polymer blends [37]. Among these, liquid crystals and leuco dyes [38, 39] are most commonly used for accurate temperature management in industry, medicine, personal care, and engineering applications [40–47]. They have been used to enhance security features to deter counterfeiting [48, 49], for marketing by imparting unique visual effects [50], and as energy-saving coating materials [41] such as smart windows or roofing [40–42]. Additionally, thermochromic fibers have been used to make smart textiles and wearable devices that serve as human-machine interfaces where the machine presents data to the user via color change display [45, 51]. For example, thermochromic textiles have been used to monitor drug release kinetics from epidermal patches. $\text{Fe}_3\text{O}_4@C$ magnetic nanoparticles doped poly (N-isopropylacrylamide-co-acrylic acid) (PIPAM-AAc) prepolymer was used to coat a spandex fabric and polymerized using UV-radiation under the influence of a magnetic field to make the patch. The magnetic field is used to align the iron nanoparticles so that this defined alignment imparts a bright color to the hydrogel. The patch is then impregnated with antimicrobial drug complexed with β -Cyclodextrin in order to serve as wound dressing fabric [52]. This hydrogel swells at room temperature and shrinks at physiological temperature or above, and this swelling-shrinking process causes drug to be loaded and released from the fabrics. This swelling-deswelling process also causes the lattice spacing of the nanomaterial to change, which imparts color change—thermochromism. Similarly, thermochromic liquid crystal (TLC) incorporated into the fabric of socks report thermal patterns of the foot to provide early warning and an opportunity to clinically manage and prevent diabetic foot ulcerations [53, 54]. In the pharmaceutical industry, thermochromic inks facilitate monitoring of the drying process of pharmaceutical formulation to avoid thermal stress of heat-sensitive active ingredients [55] or to monitor the storage temperature of medical or food products during transportation or storage [56].

While all thermochromic materials change color with temperature, they can be classified as “irreversible” (color changes permanently once exposed to higher temperature [44, 57]) or “reversible” (regain original color after cooling to the original temperature) [58–61].

Reversible thermochromic inks

Reversible thermochromic inks change their color upon heating and regain their original color on cooling. They consist of three components: namely a color former, color developer and solvent. Color formers are electron donor, spacer, and acceptor organic compounds such as N-acyl-leuco-methylene blue derivatives, diary phthalides, diphenylmethanes, spiro lactones, fluorans, Spiro pyrans or fulgides, whereas color developers are electron donor or acceptors chosen to interact with the color former [62–65] to develop a unique color. These tricomponent mixtures (color former, developer and hydrophobic nonvolatile solvent) formulated and microencapsulated in translucent and impermeable polymeric material behave as a thermochromic ink [66, 67]. Before heating, the color former and developer remain separated in the polymeric material. Upon heating, the polymeric material dissociates, and the color former and developer homogeneously mix within the solvent which leads either to color loss or development. Recently, a tricomponent mixture of reversible thermochromic ink based on bipyridinium polyelectrolyte (color former) reported a thermochromic transition temperature in the range of 45–105 °C [62]. The polyelectrolyte interacts with different electron donors (color developers) in the presence of water (solvent). Water molecules are bound to the polyelectrolyte with varying strength, and the weakly bound water, coupled with the interaction of π -stacked donors, are responsible for thermochromism. Thermochromic

reversibility results when the polyelectrolyte (blue color) interacts with the different electron donors (red color) and water (Fig. 1).

Another example with similar mechanism is color development of fluoran dye. At room temperature, the color former fluoran dye exists as a dipolar molecule consisting of carboxylic acid and highly conjugated cationic moiety. This dipolar dye stabilized by electron donor (color developer, e.g., lauryl gallate) compounds and solvent, long chain alcohol (R-OH) and appeared to be reddish (Fig. 2). However, heating results in molecular rearrangement leading to lactonization of this dye, eliminating the conjugation (π - π electron density), displacing the developer, as a result fluoran dye undergoes colorless thermochromic transition [63, 68, 69]. Leuco dye-based color formers can be inorganic, organic, or a mixture of both [70]. Inorganic thermochromic materials are composed of metal iodide, coordination compounds or double salts of mercury, silver, cobalt, nickel, vanadium, tungstate and copper [33]. The thermochromism of these compounds arises from thermally-induced changes in crystalline phase, ligand geometry, the number of ligands or solvent molecules from the coordination sphere (addition or decomposition or removal of low boiling components from the coordination) [33]. For instance, heat transforms the square planar geometry of hexaaquacopper (II) complex into tetrahedral geometry of tetrachlorocuprate (II) anion in the presence of chloride salt (Fig. 3) as a result providing its thermochromic reversibility, i.e., from blue to green. Non-pigmented thermochromic ink was also recently fabricated from polydiacetylene (PDA, photopolymerized from diacetylene monomer). The color-forming component, PDA, undergoes a transition to blue-to-red color upon exposure to a stimulus, such as heat, chemical, or mechanical stress [71, 72]. The

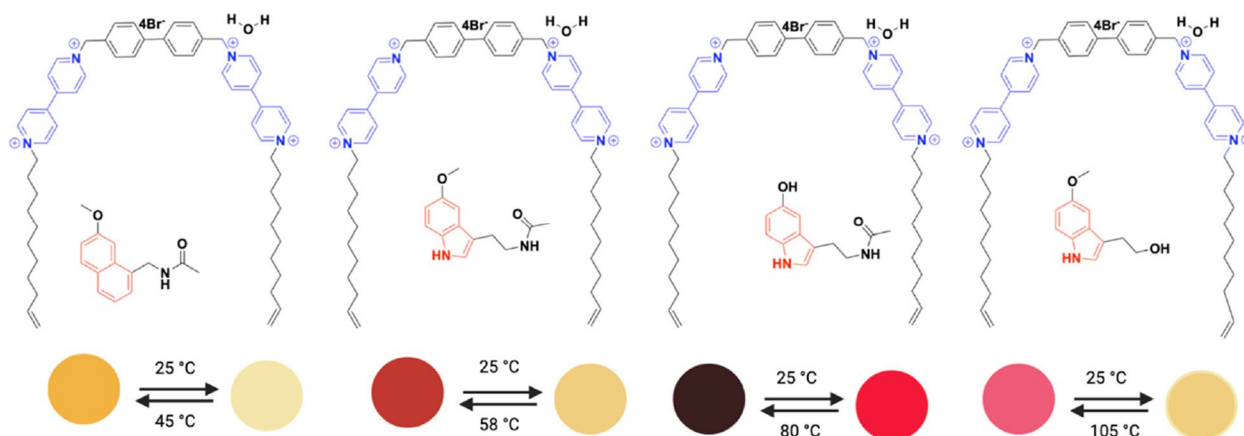


Fig. 1 Amphiphilic Bis-bipyridinium π -Acceptor (blue) interacts with π -Donors (red) and water molecules to assume thermochromic property with temperature changes. Thermochromism and thermochromic transition temperature for each complex shown at the bottom

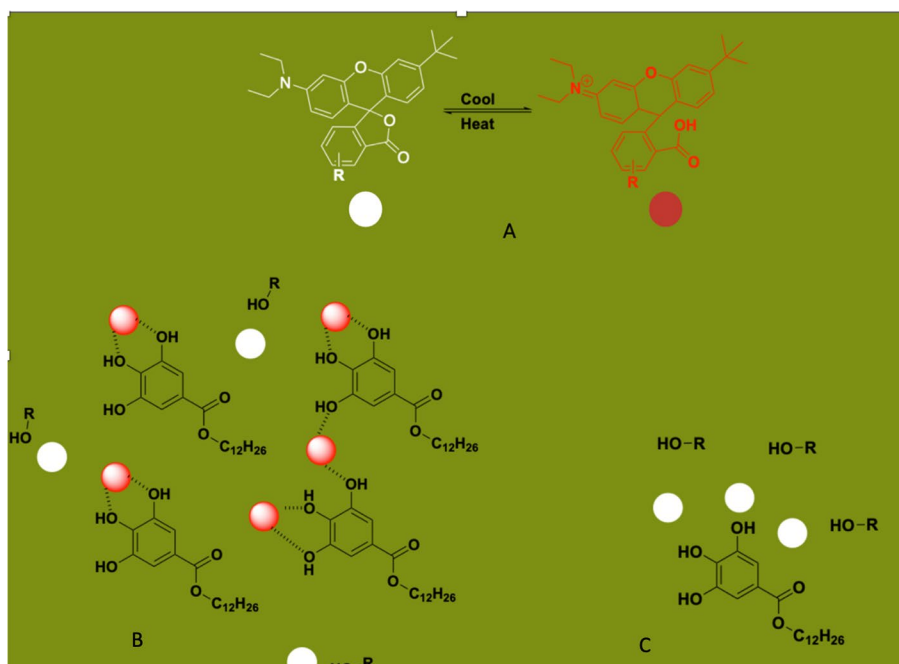


Fig. 2 Schematic view for thermochromic response of fluoran-gallate system: **a** Thermochromic effect of fluoran to heat and cooling. **b** Leuco dye (fluoran, white circle), developer (gallate) and solvent (R-OH) before commencement of heat where interaction of fluoran and gallate occurs at ambient temperature showing development and stabilization of color development; **c** Heat causes lactonization of the fluoran and eliminating interaction with developer and solvent

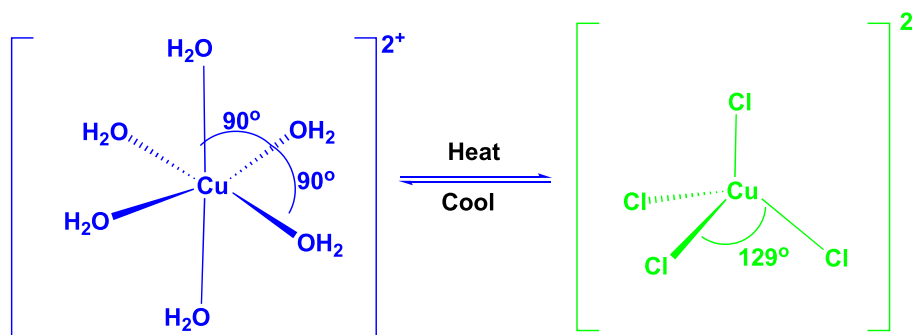


Fig. 3 Reaction scheme and structures where thermochromic property of copper complex displayed as the blue hexaquaquacopper (II) when heated, changes to green tetrachlorocuprate (II) and reverts upon cooling [70]

blue-to-red color transition upon the action of stimulus is due to a shortening of the π -conjugated bonds [36] compared to the high electron density of PDA which has trans-configuration (Fig. 4).

Products derived from these types of inks have found uses in defining the expected outcomes of TA procedures. For instance, to report the success of an infraclavicular brachial plexus block procedure which results in vasodilatation in cutaneous arterioles, and hence increases local skin temperature; thermochromic nail

polish was applied to detect a change in skin temperature [73]. Reversibility makes these types of inks useful in the above applications and are appealing for specific TA applications (such as monitoring time-dependence of body surface temperature). However, more commonly irreversible inks are desirable for formulating TMTCPs to characterize TA devices and report maximum achieved temperatures in an in vitro experiment as these phantoms provide lasting thermal event mapping properties.

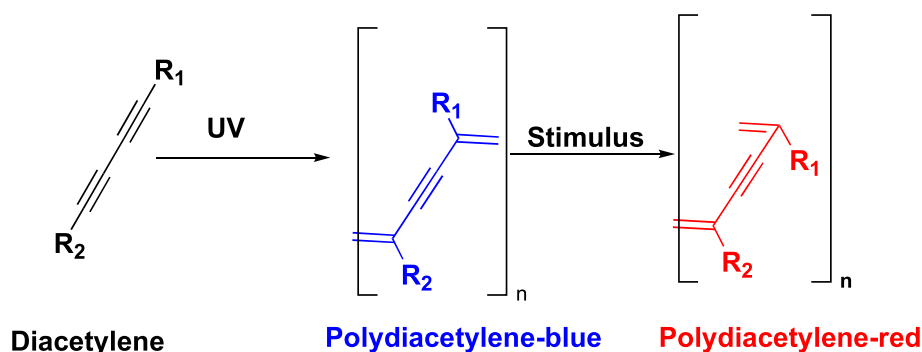


Fig. 4 Assembly of polydiacetylene and its transition from blue to red due to stimulus

Irreversible thermochromic inks

Irreversible thermochromic inks are also composed of leuco dye, color developer and solvent. Like the reversible thermochromic ink, the ink is microencapsulated to prevent direct access of the dye with the developer or solvent. Their thermochromism is a result of permanent color change upon heating. As the temperature rises, color former and color developer leak from the polymer coat, intimately mix with the solvent leading to permanent color change because of molecular rearrangement of the dye. For instance, organic salt of sulfonated anils, specifically, 2-[(2-hydroxy-3-methoxy-benzylidene)-amino]-benzenesulfonic acid forms hydroxylate[−]pyridinium macromolecule interacts with 4,4'-bipyridine to develop permanent color change [74]. The color transition is from brown at room temperature to red upon grinding and brick red when heated. PDA can also be modified to permanently change its color upon heating. Colorimetric irreversibility of PDA is achieved by introducing molecules that lead to headgroup interactions (both hydrogen-bonding and aromatic interaction) on the acyl side chains [75–78]. These types of irreversible inks are desirable for modeling in vivo ablations when incorporated into tissue-mimicking phantoms to allow spatial reporting of maximum temperature changes during in vitro ablation, discerning ablation morphology (size and shape), characterizing thermal devices and planning treatment.

Thermochromic liquid crystals

Thermochromic liquid crystals are a type of liquid crystal made of anisotropic molecules whose molecular interactions due to heating promote change in directional and positional orders. Therefore, their color transitions can be due to changes in crystalline phase and molecular orientation [70]. Crystals may point in the same direction (no positional order) without being layered so that molecules are free to rotate (rotational order) or slide past one another (Nematic phase) or aligned in layers

enabling rotation about their long axes within a given plane without sliding past one another (Smectic phase) or twist around a fixed axis. Both nematic and smectic liquid crystals do not exhibit thermochromism as they are not optically active [79]. In cholesteric phase, usually called chiral nematic phase, molecules are directionally oriented (director, n) and piled (positioned) in a spiral pattern, with each layer rotated at a slight angle (θ) to the ones above and below [80] changing orientation when heated and become optically active. As a result, these molecules exhibit thermochromism. The cholesteric liquid crystals are characterized by the following important parameters (Fig. 5): director, n which is a long-range orientational order along a preferred direction, a pitch (P) a distance along the helix over which the director rotate by 360° and θ , a twisting angle of the helix [81]. When orientation changes in response to change in temperature so as their interaction with light leading to change in color [60, 82]. Thermochromism of thermochromic liquid crystals (TLCs) is, therefore, a result of a temperature-driven crystal phase changes. Currently TLCs are available in the form of pure, unencapsulated aqueous slurries and pre-made sheets, and microencapsulated TLCs. Even though pure TLCs have short shelf life, due to degradation which result in contamination, they provide brilliant color and high spatial resolution temperature field [83]. On the other hand, microencapsulated TLCs are encased within spherical polymer capsules and are chemically stable. These TLCs are manufactured in water-soluble and water-resistant form and mixed with adhesive polymers where they can be applied on a clean surface as a sprayable coatings. Alternatively, microencapsulated TLCs deposited on premanufactured sheets and stuck on clear polyester sheet on a black background that has pressure-sensitive adhesive. This can be readily attached onto the desired surface and ready for TA device calibration and characterization and report temperature distribution in accordance with their change in color [84].

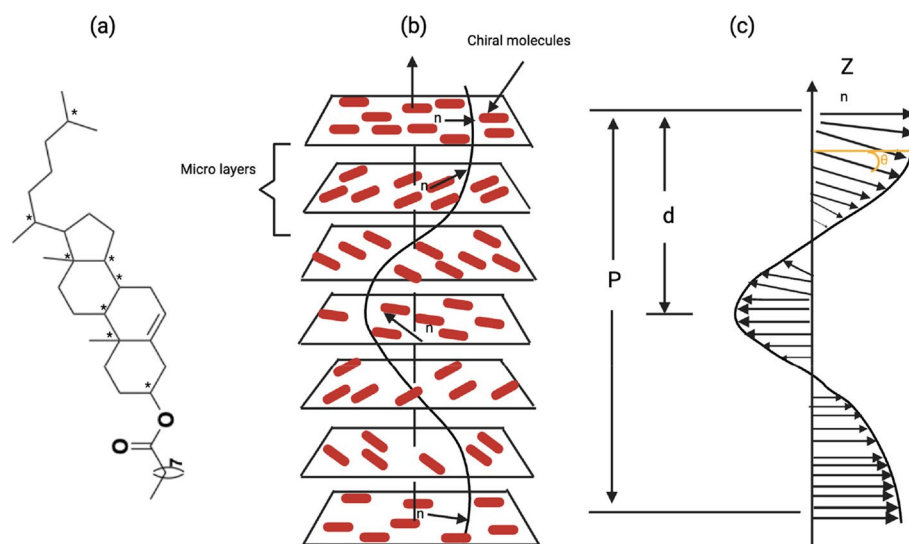


Fig. 5 Chiral Nematic (cholesteric phase) liquid crystal forming cholesteric liquid crystals with helical structure. **a** cholesterol derivative with eight chiral centers (*), **(b)** spatial and directional arrangement of chiral molecules (Red rods); each layer is rotating with respect to the ones above and below it to give a spiral structure, i.e., they have a preferential twist arrangement with respect to one another; **(c)** long-range orientational ordered (n) along a preferred direction of cholesteric phase; where n , P , d , and θ indicate, orientational direction of molecule about a common axis (director), pitch (the distance along the sinusoidal over which the director rotates by 2π or shift in alignment), distance ($P/2$), rotational (twisting) angle of the molecules and chiral centers, respectively

When it is incorporated in wearable fabrics, also serves as a point-of-care device for wound monitoring by measuring the temperature distribution on the wound site and the surrounding healthy skin which reduce hospitalization times, patient suffering, and cost [85]. In addition, in recent years thermochromic liquid crystals (TLC) were employed to calibrate temperature outcome for optimization of minimally invasive ablation devices [86–90].

Irreversible tissue-mimicking thermochromic phantoms

Irreversible tissue-mimicking thermochromic phantoms inform ablation planning and enable optimization by reporting temperature distribution in relation to a specific ablation probe or dependent variable [18, 91–95]. They are composed of base material such as acrylamide gel, polyvinyl alcohol (PVA), or silicone combined with thermochromic ink ($\geq 1\%$) and other additives. The base materials provide tissue-like property while the ink and additives serve as a temperature probe and an electrical conductor (or ultrasound absorber), respectively. In these phantoms, the ink permanently changes color from crème white to magenta (Fig. 6, left). The color transition begins at 40°C and magenta becomes most saturated at 68°C and above, allowing for quantification of temperature as shown in Fig. 6 (right) [18–20, 93–95]. The extent of the color change for irreversible thermochromic materials depends only on the maximum temperature achieved, and not on

the rate of heating or on the duration of exposed temperature. The threshold temperature of a color-changing thermochromic phantom depends on the thermochromic ink used to formulate the phantom. It ranges from 50 to 200°C and exhibit a color change upon change in temperature (<https://spotsee.io/products/temperature/heatmark-indicator-inks-pigments-coatings/>). For instance, the acrylamide-based thermochromic phantom in tubes, change colors in response to different temperatures when bathed in water from 30 to 75°C [96] (see Fig. 6)

Thermophysical properties of phantoms given the addition of various additives to customize formulations towards optimization for use with specific ablation methodology and modalities are described below [19, 20] and detailed in Tables 1 and 2. These phantoms respond to change to temperatures from 40 to 68°C and have also acoustic and thermal properties similar to those of human liver tissue [72, 97] (Table 1). Temperature changes are visualized by sectioning the TMTCPs along planes of interest (e.g., parallel to the ablation probe at increasing distances from the center) and imaging with a standard optical camera. Mapping between the color change and the maximum temperature reached can be achieved by comparing the color intensity with that of TMTCPs heated to a known temperature in a water bath or oven with temperature-measuring capability. This temperature range is relevant to the bio-effects intentionally induced by medical hyperthermia and thermal ablation.

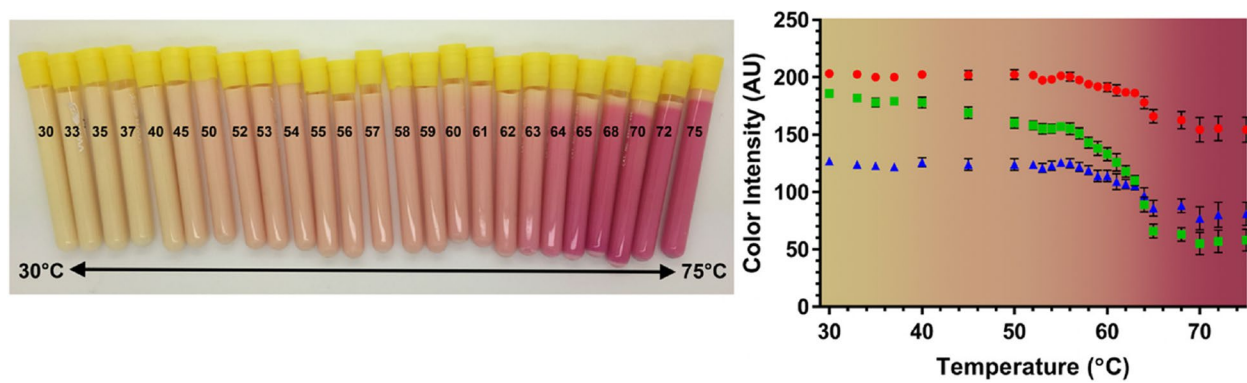


Fig. 6 Color-changing thermochromic phantom based on acrylamide gel with changes in temperature. Phantom in tubes water bathed from 30 to 75 °C (left); Red (circle), green (square) and blue (triangle) intensities vs. temperature curves derived by quantifying RGB color intensity values of the TMTCP samples as a function of temperature between 30 and 75 °C, overlaid on a computer-generated color swatch. Tissue-mimicking thermochromic phantom for characterization of HIFU devices and applications© 2019 by Avinash Eranki is licensed under Attribution 4.0 International

Table 1 Physical and thermal properties of TMTCP and acrylamide base phantom

Physical and thermal properties ^a	TMTCP (test conducted prior to heating) [18, 19]	Acrylamide phantom [26]	Soft tissue-liver [98–104], (https://itis.swiss/virtual-population/tissue-properties/database/)
Density	1033 ± 1 kg/m ³	1000-1070	1079
Thermal conductivity (W/m/K)	0.58 ± 0.01	0.56-0.65	0.44-0.59
Electrical conductivity (S/m)		1.19-2.26	0.48
Thermal diffusivity (mm ² /s)	0.143 ± 0.002		0.14 (@37°C)
Speed of sound (m/s)	1522 ± 5		1568-1585
Acoustic impedance (kg/m ² s)	1.575 ± 0.005 × 10 ⁶		1.6 ± 0.01 × 10 ⁵
Acoustic attenuation (dB/cm/MHz)	0.23 ± 0.02		0.23-0.73
Dielectric constant (ε _r)		48-58	50.8 ± 4.1
Specific heat capacity (kJ/kg/K)		3.59-3.93	3.5
T2 relaxation time at 1.5T/3T (ms)	225 ± 14 / 152 ± 8		56.4 (1.5T)

^a Formulation dependent

Table 2 Different irreversible tissue mimicking thermochromic phantom formulations and their respective compatible heating devices

Thermochromic phantom containing	Compatible heating device				
	Laser	RF	MW	HIFU	Note
Acrylamide gel + Ink only [18]	✓		✓		
Acrylamide gel + Ink + salt [20]	✓	✓	✓		
Acrylamide gel + Ink + BSA [91]	✓		✓		Relative temp. Could also be monitored using MR (from BSA coagulation)
Acrylamide gel + Ink + SiO ₂ [19]	✓		✓	✓	
Acrylamide gel + Ink + BSA + Salt [19]	✓	✓	✓		Relative temp. Could also be monitored using MR (from BSA coagulation)
Acrylamide gel + Ink + BSA + Salt + SiO ₂ [19]	✓	✓	✓	✓	Relative temp. Could also be monitored using MR (from BSA coagulation)
Polyvinyl alcohol + INK+NaCl [95, 97]	✓	✓		✓	
Silicone + INK [26]				✓	
Agar + INK + egg yolk + Salt [23]		✓			
Polydiacetylene, agar and lipid [75, 76]				✓	
Thermochromic liquid crystal [105–108]	✓	✓	✓	✓	

Thermal ablation devices and the corresponding thermochromic phantom formulations

Radiofrequency (RF), Laser, Microwave (MW) and high intensity focused ultrasound (HIFU) are clinical thermal ablation devices [1]. The main challenge to characterize these TA devices is the lack of biomimetic systems that report ablation and temperature without using in situ thermometer or expensive and complex ex situ temperature monitoring devices like magnetic resonance (MR) imaging thermometry. Recently different biophysical models such as thermochromic phantoms have been used to characterize different TA devices and are summarized in Table 2.

Radiofrequency ablation devices

RFA has been the most widely used tumor-ablation technique for percutaneous treatment of unresectable or oligometastatic solid tumors [109]. RFA can effectively ablate large and irregular tumor either by multitined expandable electrodes or perfused electrodes to prevent charring and vaporization which limit thermal conduction [110, 111]. For example, innovations in electrode design such as perfused clustered, expandable, multitined, and multipolar [112], monopolar with a multiple electrode switching system [113], and a multiple switching system [114] enable safe and efficient ablation therapy. Their use on small to medium-sized tumor in HCC patients resulted in excellent local tumor control with high rate of tumor progression-free survival as they provided adequate ablation volume [113].

RFA's complete ablation and local efficacy depend on achieving an adequate ablation temperature throughout the planned treatment volume to encompass the target tumor tissue. Planned treatment volume is in

part determined by the proper placement of the needle, the amount of energy deposited, the number of ablations per session and the tumor size [115–117]. Needle placement is guided by various intraoperative imaging methods such as Computed Tomography (CT) [118] or ultrasound [119]. However, accurate needle placement alone cannot guarantee efficient ablation, as tissue conductivity and heat loss due to perfusion also play a role. TMCTP have been employed to evaluate the thermal properties of RF ablation device (e.g., maximum temperature achieved at the electrode-tissue interface), determine the extent of thermal injury (defined by margin depth, width and circumferential coverage), and to compare ablation outcomes with ex-vivo and computational models [105, 120–122]. In these applications, a similarity in shape and volume (ellipsoid) is noted between RF-ablated ex vivo liver (as observed from the visual assessment of thermally coagulated tissue) and RF-ablated thermochromic phantoms (visual evaluation of color depth and color gradient) [20]. Measurements of the temperature profile at distances of 0.5, 1.0, 1.5, and 2.0 cm from the ablation probe revealed that the rate of heating is similar for TMTCP and ex vivo tissue until the onset of tissue charring which then leads to an increase in impedance and a plateau in the temperature recorded by the most proximal measurement probe (Fig. 7). Maximum temperatures and heating profiles for measurement probes of 1.0, 1.5, and 2.0 cm away from the ablation probe were nearly identical between ex vivo tissue and TMTCP. These results clarify the value of TMTCP for predicting the heating behavior and size of lesions created by RFA. However, one limitation is that TMTCPs do not recapitulate tissue charring within 0.5 cm of the ablation probe (and resulting reduction in thermal

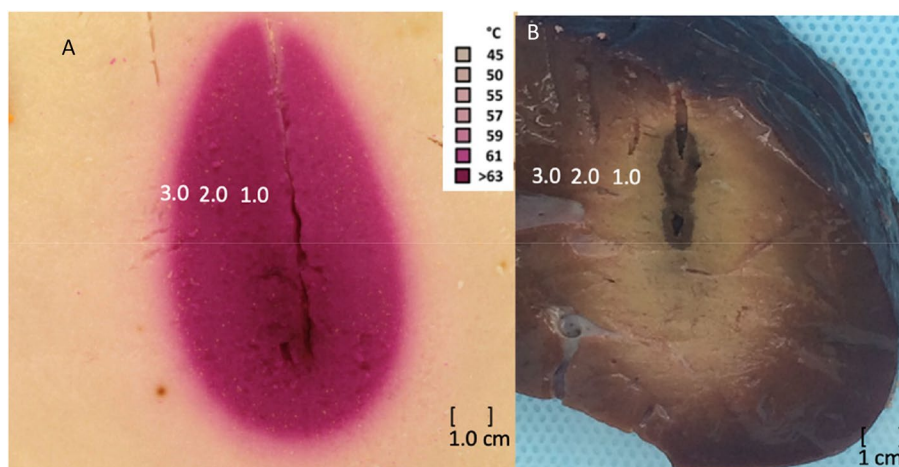


Fig. 7 Cross sectional photograph of (a) TMTCP and (b) ex vivo bovine liver along the electrode following RF heating. The optical temperature probe tips are placed at distances of 0.5, 1.0, 1.5, and 2.0 cm away from the RF needle

conduction. Temperatures relatively remained constant, in the ex vivo liver due to carbonization of the tissue (which resists heat flow) proximate to the electrode [20] (Fig. 7).

To improve ablation outcomes and accurately characterize RFA devices; computational models and vessel-containing phantoms have been utilized. Various computational bioheat models integrated with COMSOL Multiphysics software have been developed that consider the dependency of temperature rise and ablation zone on tissue physical properties [123]. Tissue-mimicking thermochromic phantoms have been instrumental in the validation of these models as well. The predicted lesion dimensions for this model were within 5% of the experimental phantom-based result [124]. These models are capable of automatically recomputing and adjusting parameters in response to updated tissue properties caused by temperature rises or tissue damage, informing the proper input correction. Although such sophisticated computational model needs validation, both experimentation using the phantom and simulations demonstrated similar outcomes of ablation using a given ablation device [125]. TMTCP however, does not recapitulate charring of tissue at temperatures above 95°C, at which point conductivity decreases and temperatures plateau [126]. However, since temperatures above 60°C cause irreversible cell death, computational models that predict the distribution of temperatures between 45 and 60°C will provide more accurate results. The heating behavior of healthy, “background” tissue surrounding a tumor may impact the heating profile or dynamics. Two-compartment, agar-based phantoms have been successfully implemented to determine the impact of background tissue on tumor heating during RFA. In particular, they demonstrated that background tissue with a lower thermal conductivity produces an “oven-effect” that leads to greater heating within the targeted tissue [127]. TMTCP and computational modeling could be integrated in such a 2-compartment model to better understand the impact of surrounding tissue on ablation-induced temperature increases and thermal lesions.

One of the major drawbacks of TMTCPs is the lack of perfusion, which serves as a heat sink during ablation. To investigate the impact of perfusion, TMTCPs were fabricated with vessels of different channel radii, by inserting tubes of different sizes into custom-fabricated containers before pouring the TMTCP materials and later the tubes were removed once the TMTCP was solidified. The tubes serve as vessels for saline flows at different rates [128]. As expected, ablation zone morphology depended on vessel radii and saline flow rates. With the same energy input, the ablated area decreased, as the flow rate increased, for vessels with smaller radius (0.275 mm). However, when

a temperature-based feedback algorithm was implemented that responded to changes in flow rates (high) and vessel radii (0.9 and 2.3 mm), it caused a closed-loop (self regulates to maintain a desired set point) increased energy input on the RF needle, which corroborated with an increase in ablated area. This indicated that TMTCP may customize or optimize the RFA algorithms, towards better ablation outcomes. As expected, relatively larger and symmetrical ablated areas with respect to the needle were observed for reference vessels with no flow rate, because there was no convective heat loss due to “heat sink” effect.

TMTCP are also valuable in optimizing accurate RF needle placement and estimating the ablated volume. In this application ultrasound (US) compatible thyroid nodule phantoms containing thermochromic dye were used to test the accuracy of 3D matrix US transducer guidance in optimizing accurate RF needle placement and to estimate ablated volume. The results indicated that 3D matrix transducer guidance improved the accuracy of nodule volume estimation, and reduced RFA procedure time by guiding needle placement [129].

Beyond tumor ablation, TMTCP have been implemented to optimize myocardial ablations and thermal denervation therapies. Chik. et al., created myocardial phantoms to optimize myocardial ablation that were made from a polyester sheet coated with thermochromic microspheres, and stacked in a vertical position within tissue-mimicking gel. This study demonstrated similarity between the predicted lesion dimensions from TMTCP with in vitro bovine myocardial tissue and in vivo bovine myocardial lesions post necropsy; thereby validating the use of 3D-thermochromic liquid crystals to characterize RF electrodes [130].

Renal denervation with RFA may be used to treat drug-resistant hypertension [131], with a clinical need to develop more efficient RFA catheters and better characterize the resulting lesion dimensions. To assess denervation thermal therapies, TLCs were utilized in a renal artery phantom model to compare lesion size (depth and width) that resulted from multielectrode renal denervation systems (Symplicity Spyral) and the first-generation multi-electrode system (EnLIGHTN NGE) [132]. In this study, the TLC phantom was used to compare lesion depths between multi-electrode systems, as observed from the color gradient [132]. Better predicting lesion depth may enhance efficacy of renal artery denervation in clinic and may better inform the operator on customized device selection based on the prevailing clinical scenario. In another denervation application, a radiofrequency bipolar electrode can be assembled into an endovascular “basket catheter” for deployment inside the renal artery. This catheter aims for induction heating between

60 and 100 °C [92]. To characterize and validate this RF catheter, TMTCP was used [20] together with different computational methods [92]. The temperature at the electrode-tissue interface, extent of lesion coverage, and a comparison of the extent of thermal injury for branch versus main vessel during ablation were verified and validated using a renal artery phantom containing TLC [86]. These studies informed a TLC phantom investigation of the effect of Ohmic heat on adjacent tissue in the ex-vivo esophagus, due to the presence of metallic implant near to RF ablation region. Accordingly, they observed amplified current density around the implanted metal and the ablation catheter, which resulted in heating of phantom or tissue above 45 °C around the implanted metals. Clinically, such an effect could damage nearby healthy tissue [133]. In contrast, insulating the metal implant near to the ablation devices prevented collateral heating of healthy tissue (and color change on the phantom). This color change may have informed device design requirements and insulation or proximity constraints for methods of use, to enhance safety and reduce the risk profile.

TMTCP may also find value in optimizing and characterizing new RFA devices. For instance, conventional RF catheter ablation for arrhythmia requires stable catheter position for optimal contact in the target region. However, lateral catheter sliding is a common problem that causes inadequate tissue contact, compromises lesion, and creates inconsistent lesion dimensions that can even lead to perforation [134]. These challenges were addressed using thermochromic gel myocardia phantom to show that a gated pulsed RF catheter delivered consistently deeper lesions and a faster ablation, irrespective of the degree of catheter movement, in comparison to conventional RF catheters [135]. This study illustrates the use of thermochromic phantoms in characterizing new RF technologies prior to their use in vivo testing or in clinic.

TMTCP-reliant models were used to simulate and experimentally validate the use of RFA for the treatment of Cerebral Palsy [136], by combining TLC-containing homogeneous gel phantom with COMSOL Multiphysics model, an adaptive tool widely used to test RF probes in complex biological environments.

Since RFA relies on conduction of electricity to generate heat, TMTCPs with different additives have been formulated to match specific needs and questions. Electrical impedance adjustable thermochromic tissue-mimicking phantom for RFA were formulated with egg yolk (23%), agar powder (68%) and thermochromic ink (9%) and different salt concentrations to reflect different tissue types [23]. This phantom enabled distinct visualization of tissue area treated at or above 60 °C, similar to other formulations. However, a major drawback of this phantom lies on the type of agar used, which could either be a low

or high boiling agar. If low-melting agar is used the phantoms are less stable to the ablation temperature of the needle, and potentially melt when they reach high temperatures greater than the melting point of the low-temperature agar. However, high boiling agar is not suitable because it causes premature color change to the incorporated ink as the molten agar solidifies at the temperature safest to add the ink during phantom preparation. Alternatively, thermochromic tissue phantoms made from polyvinyl alcohol containing 5% thermochromic ink may characterize the thermal effects associated with pulsed electric field treatments [120]. This phantom has similar basic composition with ultrasound therapy phantoms [95] for characterization and optimization of HIFU outcomes. Therefore, TLC formulations may be customized to better suit the ablation modality in question, to better characterize and validate TA devices or computational algorithms across a variety of TA modalities and technologies, including RFA, pulsed electrical fields, irreversible electroporation, MWA, HIFU, and laser.

Irreversible electroporation

Irreversible electroporation (IRE) and pulsed electrical fields (NanoKnife, Angiodynamics, IGEA, or Galvanize Aliya) are emerging minimally invasive nonthermal ablation procedures that deliver a series of intense but short duration electrical pulses to permanently disrupt cell membranes leading to cell death, cellular membrane permeabilization, transfection, or recruitment of tertiary lymphoid structures [137–141]. Although this technique has been misnamed “nonthermal”, high currents can in fact increase local tissue temperature as a result of the Joule heating effect [142]. Better characterization of the shape size and features of heat effects of such devices may minimize the risk for off-target thermal damage or inform better use. TMTCP serves as a tool to characterize and minimize potential tissue thermal damage while using this technology [120] as well as clarifying mechanistic studies.

Microwave ablation devices

Microwave ablation is a thermal ablative procedures that have emerged as a popular minimally invasive alternatives to surgical removal of solid tumor. It continues to evolve in terms of antenna design, reflected power, and spatial and concurrent distribution of power via multiple antennas [143, 144], and the development of multi-slot antennas with gas cooling capability [145, 146]. MWA may yield improved local control of unresectable tumors due to less convective heat sink than RFA and faster ablation volumes, thereby locally control unresectable tumors, and provide favorable survival benefit. For example, innovations on electrodes generating high power

[147], which include perfused clustered, expandable, multi-tined, and multipolar [112], monopolar with a multiple electrode switching system [113], and a multiple switching system [114] led MWA to achieve higher temperatures faster and safer, and as result a larger thermal lesion [148]. For efficient treatment of cancer using TA device; it is often crucial to create an ablation zone that extends 1 cm beyond the tumor boundary at all points [149]. This ensures complete destruction of the entire tumor; thereby avoiding tumor relapse. The ablation zone is determined by antenna design, the time-temperature profile, and modality of electromagnetic energy [150]. Thus, techniques that accurately predict and measure the transient temperature profile in tissue during ablation may better inform treatment planning. Thermochromic tissue-mimicking phantoms [18] demonstrated that MWA at 60 W for 5, 10 and 15 minutes resulted in increased sizes of 3.0×1.8 cm, 3.5×2.5 cm, and 4.0×3.5 cm, respectively with increasing time (Fig. 8) [151]. These findings indicated that if the energy deposition is kept constant, longer duration of MWA resulted in wider ablation zones. Composite ablations with multiple placements may also be performed to try to ensure coverage and assess risk.

MWA may also be applied to cardiac arrhythmias but is susceptible to inadequate or inconsistent catheter contact with the mapped target tissue and may leave “isolation

gaps” that reduce efficacy [152]. To address this unmet clinical need, noncontact microwave catheter ablation was characterized using an in vitro custom phantom model of a pulmonary vein and TLC sheets embedded in myocardium. The area of color change of the phantom allowed visualization and dynamic characterization of thermal lesions. These models also demonstrated the possibility of sparing tissue surfaces by optimizing the input power and flow rates during ablation. TLC and TMTCP thus characterized and validated specific clinical MW ablation devices.

Laser thermal ablation devices

Focal Laser Ablation (FLA) is a minimally invasive procedure employed to destroy accessible lesions using laser energy delivered via needle optical fibers placed in the center of the lesion. Each single laser ablation typically takes a couple of minutes. The boundary of the ablation zone is very sharp, making it easier to model the treatment planning. The extent of efficacy relies upon the number of fibers used, accurate segmentation of tumor boundary, maximizing the composite ablation zone and achieving the optimum tumor-killing temperature throughout the entire lesion [153–155]. The thermal threshold and size of ablated lesion during laser ablation can be monitored in real-time using MR imaging because the fibers are MR-compatible and do not create artifacts

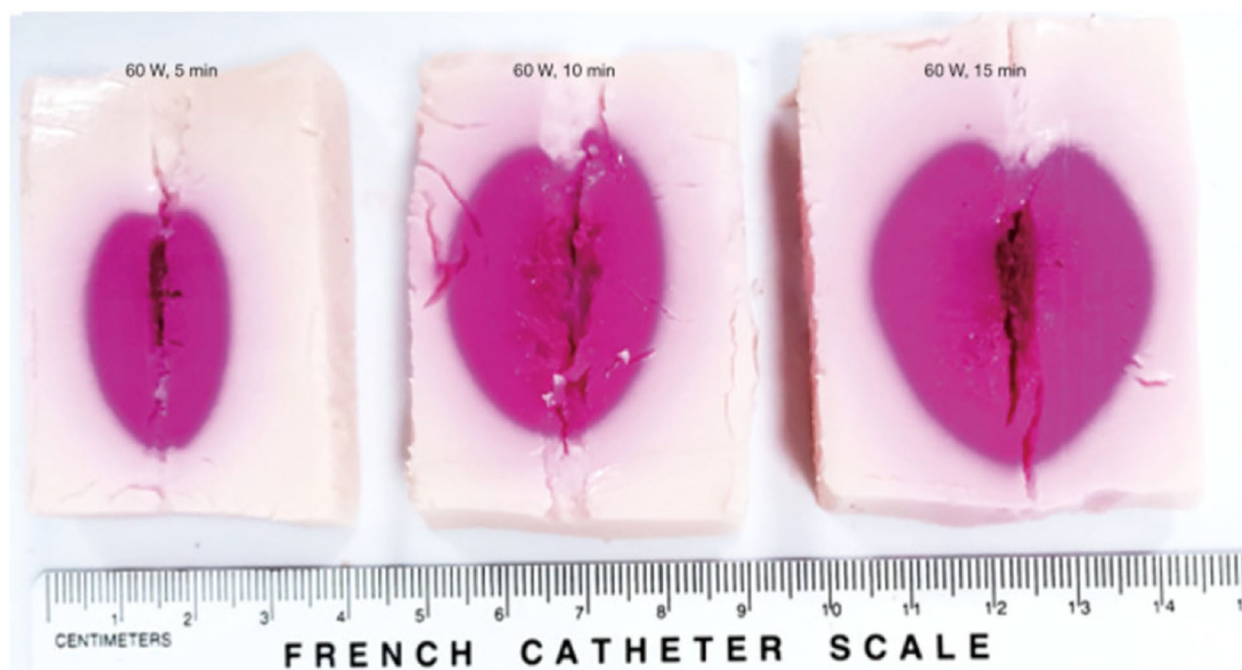


Fig. 8 The gross specimen of the phantom model after MWA showing ablated phantom with 60W at a different time. Showing an increase in ablation size with time of ablation. A thermochromic tissue-mimicking phantom model for verification of ablation plans in thermal ablation© 2021 by Yan Zhou, et al. is licensed under CC BY 4.0

[155–157]. However, MRI imaging is expensive and requires specific hardware. In a clinical suite where MR guidance and imaging is unavailable the use of thermo-chromic tissue mimicking phantom may inform and optimize energy output and ablation size for a given needle/s [158] for in vitro, and ex vivo setups that may inform clinical performances. Image guidance, treatment planning, and ablation monitoring may be integrated into one system for most ablation, including FLA. An integrated FLA system was tested using TMTCP containing bovine serum albumin (BSA) [158] which defined achieved temperature, ablation size and shape. Albumin containing TMTCP was used to validate the extent of ablation as observed from MR which corroborated with the visualized color change post-FLA. BSA was used as an additive to detect the ablation zone due to changes in transverse relaxation time (T_2) because of BSA coagulation which turns the MR image darker when the ablation temperature rose above 40°C (coagulation temperature for BSA

at its isoelectric point- [pH5.1-5.5]). The observed color change from the TMTCP due to multiple firing of infrared energy from laser fiber needle defined the shape of the ablation zone (Fig. 9) and matched the achieved temperature measured by MR (Fig. 10).

The result was also consistent with MR thermometry measurement in prostate cancer patients (data obtained from retrospective clinical study) [91]. The color change observed on the TMTCP slice matched the location and orientation on the post-ablated MR images (see Fig. 10). A similar TMTCP that did not incorporate albumin was used to validate a novel custom MR-compatible robot for MR-guided focal laser ablation of prostate cancer [159]. TMTCP and ex-vivo models thus facilitated translation and integration of custom robotics hardware and treatment planning software to create an ablation workflow that accurately targeted tumor with planned treatment volumes and margins. Analysis of agarose-based phantoms with MR-thermometry revealed similarity in the



Fig. 9 Side-firing laser fiber (left) and the ablation zone in a thermochromic phantom (right). Courtesy of Xu, et al. Xu. S.; An MRI guided system for prostate laser ablation with treatment planning and multi-planar temperature monitoring. *SPIE*. 2016;9786doi:<https://doi.org/10.1117/12.2216084>, with permission

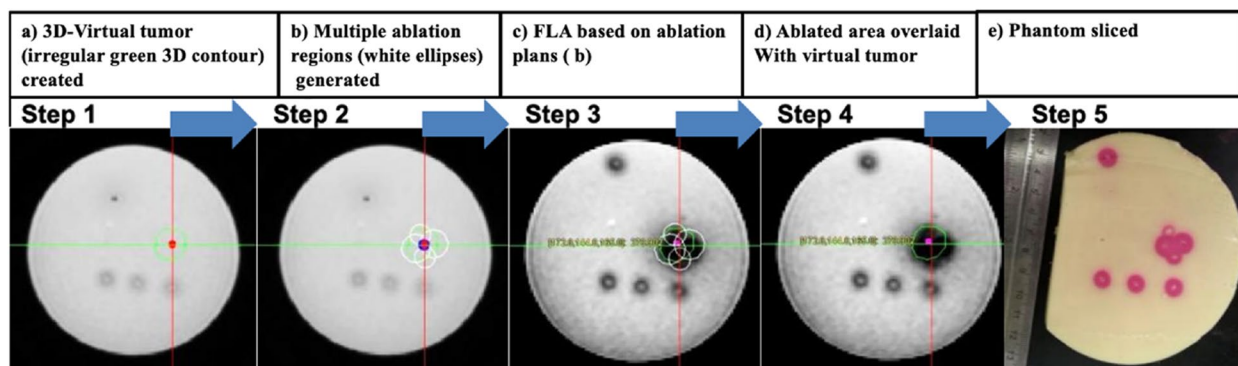


Fig. 10 a-d An abbreviated view of the steps performed to validate the system in temperature-sensitive color phantoms. The treatment area results after a single laser fiber was placed at four planned positions (white ellipses) sequentially to generate a composite ablation zone (black) to cover the tumor (green contour). **e** Temperature-sensitive color phantom sliced to match the location and orientation of the MRI scan plane. Courtesy of Xu, et al. Xu. S.; An MRI guided system for prostate laser ablation with treatment planning and multi-planar temperature monitoring. *SPIE*. 2016;9786doi:<https://doi.org/10.1117/12.2216084>, with permission

proton resonance frequency factor (PRF) with soft tissue (approximately 0.01 ppm/°C). Due to the similar high-water concentration of agarose phantoms and TMTCP, these findings encourage our confidence in the accuracy of MR thermometry for phantoms, which has been partly studied by Eranki et al. [19].

High intensity focused ultrasound ablation devices

High intensity focused ultrasound (HIFU) is non-invasive and typically delivers thermal ablation with image guidance to relatively small-sized tumor and at slightly lower target temperatures [160, 161] compared with other ablation therapies. It has been used for ablating various tumors in the prostate [162, 163], breast [164, 165], liver, pancreas, and brain [166–169]. HIFU is also used for image-guided hyperthermia-mediated drug delivery with high spatial precision using specially designed medical transducers, sensitization of tumor cell to radiation therapy, and elicitation of immune stimulation [170, 171]. The role of temperature (in either directly killing cells or modulating the tumor-immune microenvironment) motivates thermal monitoring and may require pre-procedural quality assurance to achieve the intended use in HIFU [21]. In many in vitro real-time temperature monitoring, temperature measuring probes [94, 172–178] are frequently used.

Temperature probes have limited applicability because they only measure the temperature at the point of contact with tissue in ex-vivo setting and the probe may also interfere with the acoustic field affecting the energy reaching the desired tissue [19]. On the contrary, TMTCPs [18, 95, 179] enable in vitro spatial mapping of energy deposition for HIFU ablation, hyperthermia or physiotherapy applications using inks that report ablation and hyperthermia temperatures, respectively. A newly designed hyperthermic heat delivery system was characterized using colorchanging agar-based tissue mimicking material, that changes color from 35°C to 50°C [180]. Thermal spatial mapping using TCTMP, and TLC was also employed to investigate HIFU and ultrasound for ablation and physiotherapy [19, 21, 108, 181]. Daily quality assurance of therapeutic ultrasound was achieved with a 2.8-mm-thick highly attenuating ultrasound absorber phantom layered with TLC capable of differentiating temperatures from room temperature to 40°C (black to red at 35°C, and green at 36°C, and blue at 40°C) [108]. Non-clinical TA-based experiments may monitor temperature change with multiple modalities, such as MR and US using phase transition materials like BSA containing phantoms [182]. A custom TMTCP for HIFU was developed by adding additives, such as, silicon dioxide, for attenuation of ultrasound energy and bovine serum albumin, to make the phantom visible under MR

imaging post-HIFU (Table 1) or by replacing the acrylamide/bis acrylamide [18] with polyvinyl alcohol [95, 120]. Both phantoms are useful to validate ultrasound therapy except the former may have user safety issues, such as irritation upon contact to eye, skin, respiratory tract and neurotoxicity if ingested [183]. HIFU thermal ablation of TMTCP under MR guidance resulted in permanent color changes at locations within the phantom that were exposed to ablative temperatures. The ablation size increased with an increase in ablation time (Fig. 11, top). Ablation area was also delineated on T2-weighted MR images as a permanent dark spot (Fig. 11, bottom) due to thermal coagulation of BSA [19]. Close observation indicates that the ablation size for a given time on T2 map looks larger than that observed on the color map (Fig. 11). The ablation zone variation (Fig. 11) observed from images of MR and photograph of TMTCP is due to the temperature differences between BSA starts coagulating (>40°C) at its isoelectric point (pH5.1–5.5) [184–186] and thermochromic ink starts exhibiting a full color development (>50°C). Therefore, MR detects not only the focal area (>50°C), but also the heat diffusing away from the focal area where the temperature at which BSA coagulation occurs. Whereas the color intensity of the thermochromic ink is deepened at or above 50°C [18] (HIFU focal point), it becomes undetectable as the temperature decreases away from the focal area ($\leq 40^\circ\text{C}$). The expected decrease in temperature away the HIFU focal point is illustrated on the T2 map (or change in T2 profile) and temperature contour (or color change profile) (Fig. 12). Similarly, 3D temperature distribution around the HIFU focus was visualized with a phantom made from a micro-capsulated thermochromic liquid crystal with temperature accuracy of less than 1°C and the result is comparable to MR thermometry [187, 188].

These phantom formulations thus are useful for evaluation of HIFU transducer output and quality assurance prior to use in pre-clinical and clinical settings and may reduce the number or frequency of MR calibration or test pulses. TMTCPs may function as an alternative to in vivo tumor models for preclinical testing of TA devices [189]. For instance, computational simulation and TLC-based dimensions of the focal zone and its position relative to the transducer's hardware were in agreement for a newly developed focused ultrasound system, using TLC film sensors [89]. This technique is low-cost and fast in characterizing new thermal therapy modalities. In line with this, 3D printed lumbar spine models embedded in TMTCP reproduced the ablation zone defined by MR-thermometry. To further extend the utility of the TMTCP in evaluating MRgFUS sonication, pairs of small joints in the back of the spine and phantoms of nerves around facet joints have also been studied [190]. Cost-effective

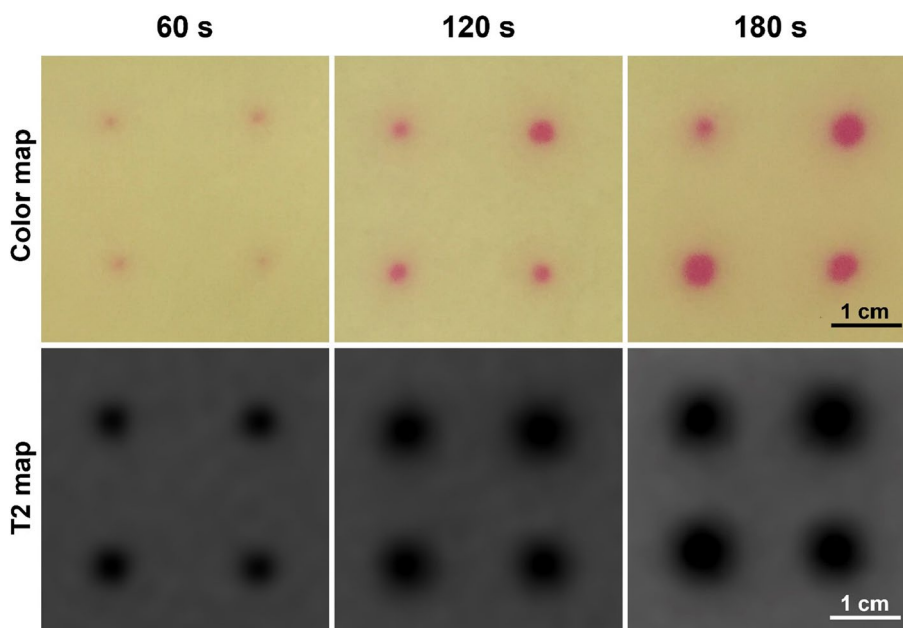


Fig. 11 Ablation size increased with ablation time, and this was observed in both the color maps and T2 maps. Courtesy of Dr. Partanen

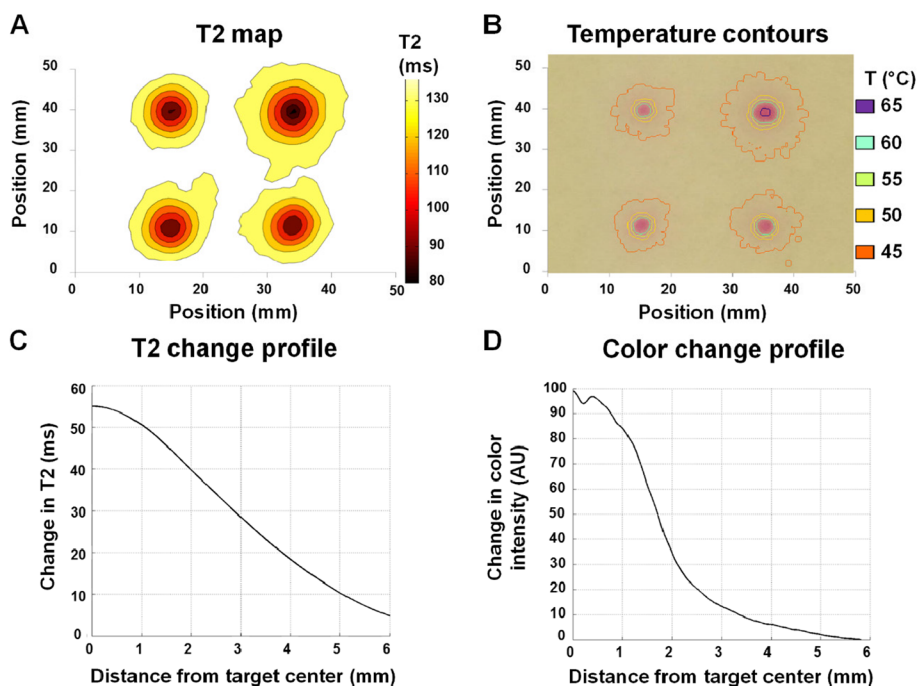


Fig. 12 Temperature decreases away the focal point of HIFU (a) T2 map, (b) Temperature contours, (c) T2 change profile and (d) color change profile. Courtesy of Dr. Partanen

and reusable PVA and silicone-based thermochromic phantom with acoustic, mechanical, and thermal characteristics suitable for HIFU have been reported [191, 192]. These materials reduce the risks of using hazardous acrylamide-based gels.

Overall, these studies demonstrate that TLC and TMTCP are used to characterize HIFU devices, troubleshoot a damaged transducer’s acoustic output (quality control), determine sonication parameters and frequency of heating to achieve sufficient ablation, all without the

need of MR imaging or physically inserted thermometry. TLC and TMTCP also provided quantitative information on absolute temperatures, ablation geometry and target accuracy from the change in color and/or T2. In addition, they both may be helpful in the design and characterization of new ultrasonic transducers. For instance, a TLC film was embedded in transparent PVA and its change of temperature elevations were used to adjust the frequency component for the optimum outcome [192] of the ultrasound devices. In general, TLC and TMTCP may detect defects or performance degradation in HIFU and US devices to reduce risk or promote efficient maintenance, while contributing towards developing quality control and calibration guidelines for clinical practice. These phantoms were also used to develop and validate new sonication probes, test therapeutic protocols to optimize the efficiency and safety before in-vivo and clinical use.

Thermochromic paint formulation and phantom to optimize therapeutic ultrasound exposures for bone cancer

Thermotherapy is a promising minimally invasive technique for bone metastases [166–170] that increases tumor temperature to inactivate and kill cancerous cells. Among thermal ablation techniques, cryoablation (CA), radiofrequency ablation (RFA) and MWA may be the most used thermal modalities to treat bone disease [8, 168, 171–173] with favorable clinical outcomes in specific settings [8, 171, 174, 175]. In contrast, HIFU enables non-invasive thermal therapy for palliative therapy for patients with bone metastasis (approval by the US Food and Drug Administration) [176]. In bone tumor therapy, applying HIFU to the targeted bone increases the temperature above 65°C resulting in tumor and nerve destruction and re-mineralization of the lesion [177]. A disadvantage of HIFU is that reflected ultrasound waves may cause critical thermal damage to the adjacent heat-sensitive organs such as untargeted nerve cells, bowel wall or skin [178]. Standard monitoring devices cannot immediately observe and predict heat diffusion and conduction around nearby tissues. Thus, the development and incorporation of bone thermochromic paint and TMTCP for in vitro ablation of bone mimic phantoms (BMP) was used to characterize HIFU and predict thermal damage to tissue adjacent to HIFU-treated bone.

Previously, thermochromic paints were employed to enable real-time temperature monitoring of engine surface temperatures [44, 193]. To extend this to bone ablations, a newly formulated thermochromic paint and a thermochromic tissue mimicking phantom were used to measure the achieved temperature of bone and surrounding phantom post-HIFU. This thermochromic paint is formulated to gradually and irreversibly change

color upon heating (ingredients provided in Table 3) [29]. The formulated paint was applied on circular BMP samples with four thin layers at 30-minute intervals between each layer to completely cover the bone phantom substrate. The painted BMP samples were dried and heated by immersing in a water bath (temperature 35–70°C with 5°C increment) for 30 seconds with a resulting color change (Fig. 13 (left)). The corresponding color density of heated BMP reference samples to varying temperatures was measured using Spectro-Guide (BYK-Gardner) spectrophotometer and plotted against temperature (Fig. 13 (right)) that caused the color density and used as a calibration sample to quantify temperatures resulting from HIFU experiments.

To minimize risk and optimize goals, a thorough understanding of the scattering of ultrasonic pressure field of the HIFU array and the extent of focal point displacement in the presence of ribcage is critical [194]. 3D printed rib phantoms either painted with thermochromic paint and embedded with tissue-mimicking acrylamide gel or unpainted bone phantom and embedded in TMTCP were used to monitor for real time temperature changes in the area surrounding rib-mimic or at target location after MR-HIFU therapy (Fig. 14) where **A** represents MRI shows the beam path, **B** shows temperature, and **C** the 240 CEM43 thermal dose contour on the rib-mimic surface after a 100 W sonication for 40 s. Quantitative and qualitative assessment of temperature rise on those location was evaluated by color change on the TMTCP adjacent to the bone in the embedded bone phantom, (Fig. 14 D) or the TMTCP painted bone phantom in bland tissue-mimicking phantom (Fig. 15). In HIFU exposed unpainted bone embedded in thermochromic phantom, a color change was observed on the TMTCP portion surrounding the bone implying overheating of the bone or diffused heat from heated bone might harm nearby tissue (Fig. 14d). These models may help characterize and optimize sonication methods

Table 3 Thermochromic paint formulation

Material	Parts by weight
Water	8.0
Ethylene glycol	3.0
Additive 8610	0.4
Titanium (IV) oxide, mixture of rutile and anatase	17.5
Magenta 60	5.0
NeoCryl XK-98	58.0
Aqueous Methocel A4M (3%, wt./wt.)	7.0
Ammonium hydroxide	0.2
Benzyl bromoacetate	0.9

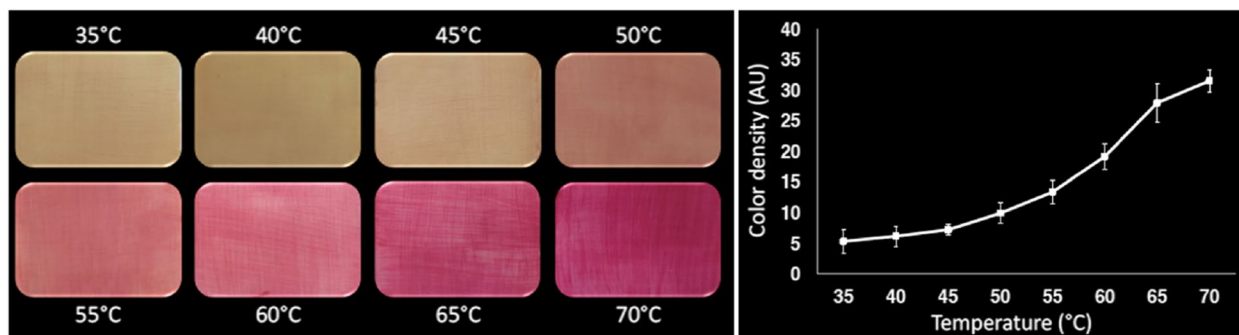


Fig. 13 Painted BMP samples heated to 35–70°C (left) and the corresponding color density of thermochromic paint as a function of temperature (right)

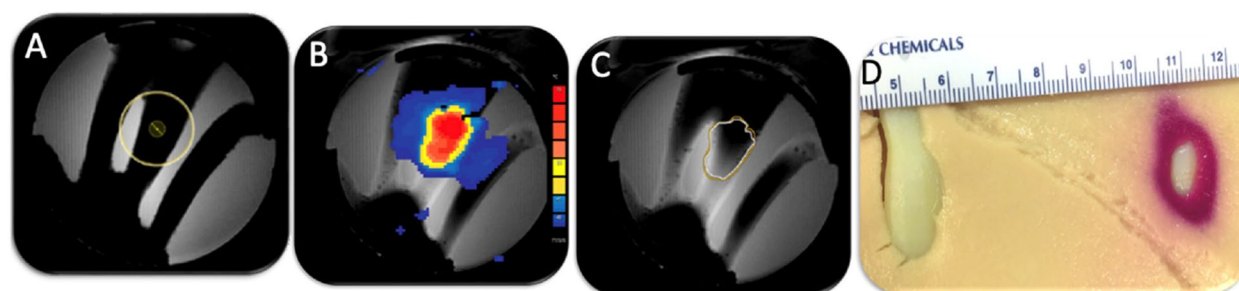


Fig. 14 Representative MRI showing the beam path (a), temperature map (b), 240 CEM43 thermal dose contour (c) on the rib-mimic surface after a 100W sonication for 40 s; and HIFU sonicated rib-mimic embedded in thermochromic phantom showing thermal damage to the nearby phantom (d)

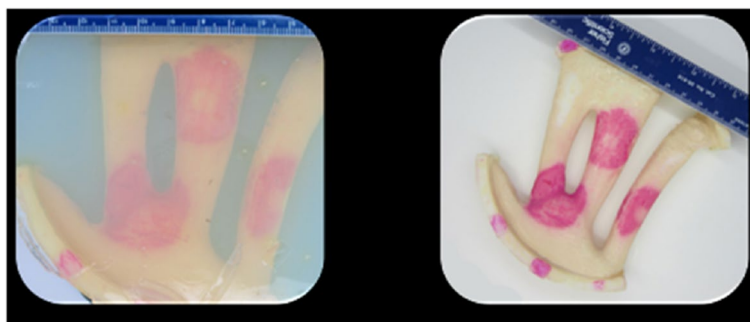


Fig. 15 Representative photos of the BMP immediately after HIFU: embedded in the gel (left), and out of gel phantom (right)

(such as HIFU exposures), development and validation of numerical models for bone HIFU therapy, or design of HIFU transducers [29, 195, 196].

Emerging uses of thermochromic phantom

Locoregional ablation generates tumor and device-specific immune-stimulatory effects [197, 198] and these effects are appealing for the potential role in systemic antitumor response [16]. Heat deposition can induce immunogenic cell death of malignant cells release of

tumor-associated antigens, as well as increase tissue permeability and blood flow to facilitate trafficking of antigens, antigen-presenting cells, and trafficking and infiltration of immune cells, or reduction of regulatory T-cells [16, 199–201]. Immune effects may be time and temperature-dependent, and elucidating an optimized ablation algorithm for immunomodulation may require a thorough understanding of the thermal profiles. Such an understanding may theoretically be facilitated by thermochromic phantoms (TCPs) that report

temperatures in the range that enhances permeability or shuts down vasculature entirely [199–202]. Certainly, the quality and effectiveness of thermal ablations need further improvement and optimization. Biomimetic materials that recapitulate in vivo tumor microenvironment may inform location, degree, and characteristics of immunogenic cell death to define drug/device strategies. Agarose-based, biocompatible, cryoprotected and color-changing (thermochromic) phantoms were developed with a modification from previously published work [18] and applications. This permitted direct visualization and quantitative determination of the temperature at which cells were exposed (data not reported). We are actively investigating the device specific immune effect of thermal ablation with methods as outlined in Fig. 16 which illustrates the workflow to isolate and quantify protein/s released from immune cells post ablation using FACS. Biomimetic phantoms may have value if able to report temperature as well as cellular and stress phenomena.

Limitations of TMTCP

For the pre-planning of thermal ablation therapies and to maximize the treatment prediction outcome, understanding of temperature dependence of tissue thermo-physical properties is necessary [99, 203]. As the intensity and duration of tissue temperature increases, bioeffects evolve. For instance, blood flow and ion diffusion

across cell membrane increase at or above 41°C [203, 204], irreversible cellular damage at or above 48°C [205, 206], instantaneous and irreversible protein denaturation above 60°C, vaporization and tissue ablation occur at or above 80°C [206, 126]. Although currently formulated TMTCPs do not inform thermo-physical properties of soft tissue mentioned above, it does inform estimated ablation volume and maximum expected temperature post ablation. Sophisticated bioheat transfer computational models include a perfusion term for convection, which is unaccounted for in a standard solid homogeneous TMTCP.

Conclusion

Thermochromic phantoms (TLC and TMTCP) and thermochromic paint may be useful for thermal therapy characterization, quality assurance of thermal devices, device improvements, user training on ablation modalities, validating acoustothermal simulations for HIFU devices, testing of new TA devices, hypothesis-driven research, and development of patient-specific 3-D models for optimization of specific TA based treatments to meet specific clinical needs. Such phantoms and paint could also provide volumetric and surface temperature information based on changes in color alone where real-time imaging or thermometry is not practicable or available. These phantoms with

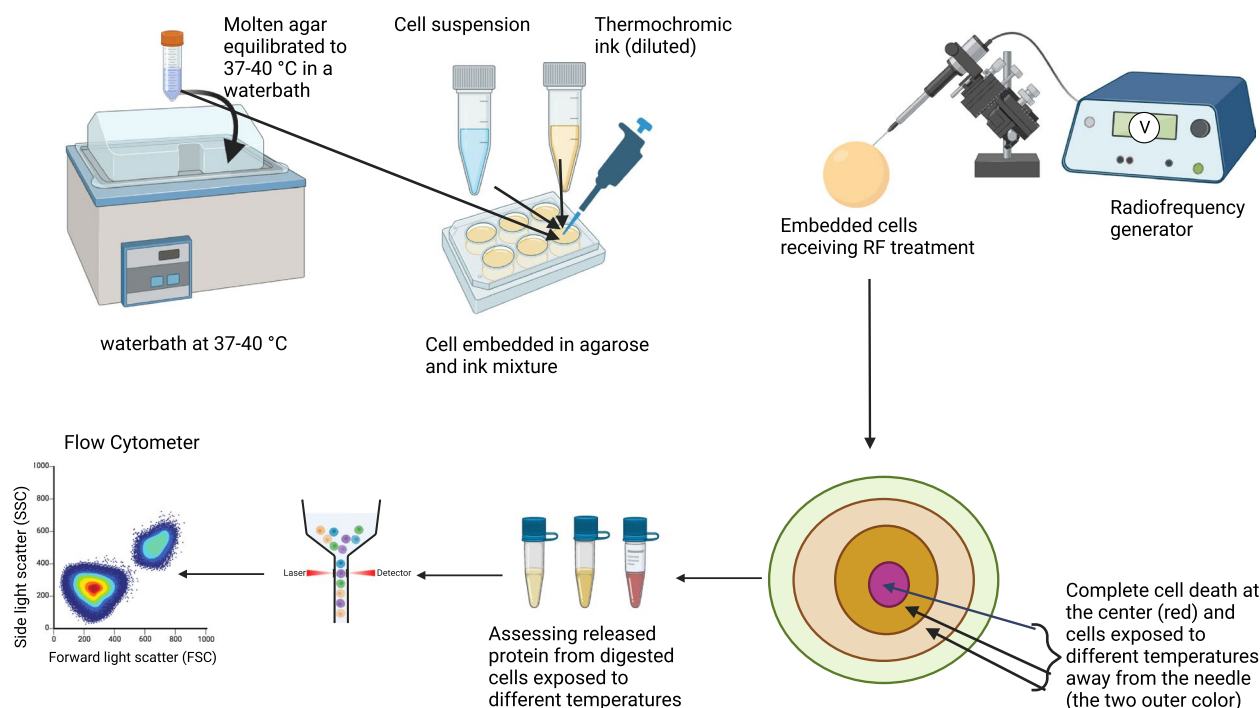


Fig. 16 Schematic illustration of proteins isolation and quantification from thermal treated cells embedded in thermochromic tissue mimicking phantom using FACS

slight modifications may be used to study the relation of immune responses to temperature changes in the context of specific temporal and spatial changes from specific thermal devices. Various experiments demonstrate that TMTCPs are also valuable as tumor models as they allow direct comparisons of ablation parameters and morphometry, different devices of the same modality, and different settings on the same device. A better modeling and understanding of the dynamic temporal and spatial temperatures following thermal ablation may inform specific applications and use temperature as a surrogate of bio-effects, across a broad spectrum of ablation devices and imaging modalities.

Acknowledgements

This work was supported by the Center for Interventional Oncology in the Intramural Research Program of the National Institutes of Health (NIH) by intramural NIH Grants NIH Z01 1ZID BC011242 and Z1A CL040015.

Disclaimer

The content of this review paper does not necessarily reflect the views or policies of the U.S. Department of Health and Human Services. The mention of commercial products, their source, or their use in connection with material reported herein is not to be taken as an actual or implied advocacy of such products by the United States government.

Authors' contributions

AHN conceived, wrote and edit the entire manuscript, prepared Figs. 1–6, and 16. RM wrote and edit. JR wrote and edit. JFD edit, SX edit and BFJW supervised all authors, gave valuable comments and edits. All authors reviewed the manuscript.

Availability of data and materials

Figures taken from existing literatures are referenced and copyright permissions are secured and stated at each figure. Any other materials used for the preparation of the manuscript are taken from our data bank are available upon request.

Declarations

Competing interests

The authors declare no competing interests.

Author details

¹Center for Interventional Oncology, National Institutes of Health, Bethesda, MD 20892, USA. ²Fischell Department of Bioengineering, University of Maryland, College Park, MD, USA.

Received: 9 November 2023 Accepted: 28 December 2023

Published: 31 January 2024

References

- H.P. Kok et al., Heating technology for malignant tumors: A review. *Int J Hyperth* **37**(1), 711–741 (2020)
- E.M. Knavel, C.L. Brace, Tumor ablation: Common modalities and general practices. *Tech Vasc Interv Radiol* **16**(4), 192–200 (2013)
- D. Li et al., Minimally invasive local therapies for liver cancer. *Cancer Biol Med* **11**(4), 217–236 (2014)
- P. Chevallier et al., Treatment of hepatocellular carcinomas by thermal ablation and hepatic transarterial chemoembolization. *Diagn Interv Imaging* **96**(6), 637–646 (2015)
- J.P. McWilliams et al., Percutaneous ablation of hepatocellular carcinoma: Current status. *J Vasc Interv Radiol* **21**(8 Suppl), S204–S213 (2010)
- Y.K. Cho, H. Rhim, S. Noh, Radiofrequency ablation versus surgical resection as primary treatment of hepatocellular carcinoma meeting the Milan criteria: A systematic review. *J Gastroenterol Hepatol* **26**(9), 1354–1360 (2011)
- S. Rossi et al., Percutaneous radio-frequency thermal ablation of nonresectable hepatocellular carcinoma after occlusion of tumor blood supply. *Radiology* **217**(1), 119–126 (2000)
- A.N. Kurup, J.M. Morris, M.R. Callstrom, Ablation of musculoskeletal metastases. *Am J Roentgenol* **209**(4), 713–721 (2017)
- R. Scipione et al., HIFU for bone metastases and other musculoskeletal applications. *Semin Interv Radiol* **35**(4), 261–267 (2018)
- A. Ademaj et al., Clinical evidence for thermometric parameters to guide hyperthermia treatment. *Cancers* **14**(3), 625 (2022)
- W.C. Dewey, Arrhenius relationships from the molecule and cell to the clinic. *Int J Hyperth* **25**(1), 3–20 (2009)
- P.X.E. Mouratidis et al., Relationship between thermal dose and cell death for "rapid" ablative and "slow" hyperthermic heating. *Int J Hyperth* **36**(1), 229–243 (2019)
- Z. Qin et al., Correlated parameter fit of arrhenius model for thermal denaturation of proteins and cells. *Ann Biomed Eng* **42**(12), 2392–2404 (2014)
- G.C. van Rhoon, Is CEM43 still a relevant thermal dose parameter for hyperthermia treatment monitoring? *Int J Hyperth* **32**(1), 50–62 (2016)
- X. He, S. Bhowmick, J.C. Bischof, Thermal therapy in urologic systems: A comparison of arrhenius and thermal isoeffective dose models in predicting hyperthermic injury. *J Biomech Eng* **131**(7), 074507 (2009)
- S.P. Haen et al., More than just tumor destruction: Immunomodulation by thermal ablation of cancer. *Clin Dev Immunol* **2011**, 160250 (2011)
- B.-L. Zhang et al., A polyacrylamide gel phantom for radiofrequency ablation. *Int J Hyperth* **24**(7), 568–576 (2008)
- A.H. Negussie et al., Thermochromic tissue-mimicking phantom for optimisation of thermal tumour ablation. *Int J Hyperth* **32**(3), 239–243 (2016)
- A. Eranki et al., Tissue-mimicking thermochromic phantom for characterization of HIFU devices and applications. *Int J Hyperthermia* **36**(1), 517–528 (2019)
- A.S. Mikhail et al., Evaluation of a tissue-mimicking thermochromic phantom for radiofrequency ablation. *Med Phys* **43**(7), 4304–4311 (2016)
- F. Qureshi et al., Thermochromic phantom for therapeutic ultrasound daily quality assurance. *Journal of Therapeutic Ultrasound* **3**(Suppl 1), 72 (2015)
- X. Zhong et al., A novel tissue-mimicking phantom for US/CT/MR-guided tumor puncture and thermal ablation. *Int J Hyperth* **39**(1), 557–563 (2022)
- L. Buehler et al., Establishment of a tissue-mimicking surrogate for pulmonary lesions to improve the development of RFA instruments and algorithms. *Biomedicines* **10**(5), 1100 (2022)
- S.R. Guntur, M.J. Choi, An improved tissue-mimicking polyacrylamide hydrogel phantom for visualizing thermal lesions with high-intensity focused ultrasound. *Ultrasound Med Biol* **40**(11), 2680–2691 (2014)
- M.J. Choi et al., A tissue mimicking polyacrylamide hydrogel phantom for visualizing thermal lesions generated by high intensity focused ultrasound. *Ultrasound Med Biol* **39**(3), 439–448 (2013)
- X. Zhong, Y. Cao, P. Zhou, Thermochromic tissue-mimicking phantoms for thermal ablation based on polyacrylamide gel. *Ultrasound Med Biol* **48**(8), 1361–1372 (2022)
- W.J. Chen, Q. Wang, C.Y. Kim, Gel phantom models for radiofrequency and microwave ablation of the liver. *Dig Dis Interv* **4**(3), 303–310 (2020)
- L. Farina et al., Thermal characterization of phantoms used for quality Assurance of Deep Hyperthermia Systems. *Sensors (Basel)* **20**(16) (2020)
- A. Negussie et al., *Thermochromic Paint Formulation and Phantom to Optimize Therapeutic Ultrasound Exposures for Bone cancer Therapy, in 34th Annual Meeting of the Society for Thermal Medicine: Systemic Treatment with Local Therapy* (Cancún, Mexico, 2017)
- B.X. Liu et al., Reversible nontoxic Thermochromic microcapsules. *ACS Appl Mater Interfaces* **12**(8), 9782–9789 (2020)
- I. Sage, Thermochromic liquid crystals. *Liq Cryst* **38**(11–12), 1551–1561 (2011)
- K. Basnec et al., Relation between colour- and phase changes of a leuco dye-based thermochromic composite. *Sci Rep*, 8 (2018)

33. J.H. Day, Thermochromism of inorganic compounds. *Chem Rev* **68**(6), 649 (1968)
34. C. Pareja-Rivera, D. Solis-Ibarra, *Reversible and irreversible Thermochromism in copper-based halide perovskites*. *Advanced Opt Mater* **9**(15) (2021)
35. H. Tamaki et al., Size-dependent Thermochromism through enhanced Electron-phonon coupling in 1 nm quantum dots. *Angewandte Chemie-International Edition* **53**(40), 10706–10709 (2014)
36. A. Seeboth et al., Thermochromic Polymers-Function by Design. *Chem Rev* **114**(5), 3037–3068 (2014)
37. A. Seeboth, J. Kriwanek, R. Vetter, The first example of thermochromism of dyes embedded in transparent polymer gel networks. *J Mater Chem* **9**(10), 2277–2278 (1999)
38. Y.K. Zhang et al., Fabrication of visual textile temperature indicators based on reversible thermochromic fibers. *Dyes Pigments* **162**, 705–711 (2019)
39. M. De Bastiani et al., Thermochromic perovskite inks for reversible smart window applications. *Chem Mater* **29**(8), 3367–3370 (2017)
40. H.N. Ji et al., Large area infrared thermochromic VO₂ nanoparticle films prepared by inkjet printing technology. *Sol Energy Mater Sol Cells* **194**, 235–243 (2019)
41. Y.M. Li et al., Core-shell VO₂@TiO₂ nanorods that combine thermochromic and photocatalytic properties for application as energy-saving smart coatings. *Sci Rep*, 3 (2013)
42. M. Parsley, in *7th Annual Symp of the IEEE on Semiconductor Thermal Measurement and Management. The use of Thermochromic liquid crystals in research applications, thermal mapping and nondestructive testing* (Scottsdale, Az, 1991)
43. L. van der Werff et al., Thermochromic composite fibres containing liquid crystals formed via melt extrusion. *J Mater Sci* **48**(14), 5005–5011 (2013)
44. C. Lempereur, R. Andral, J.Y. Prudhomme, Surface temperature measurement on engine components by means of irreversible thermal coatings. *Meas Sci Technol* **19**(10) (2008)
45. F. Fu, L. Hu, Temperature sensitive colour-changed composites. *Advanced High Strength Natural Fibre Composites in Construction* **74**, 405–423 (2017)
46. A. Hakami et al., Review on thermochromic materials: Development, characterization, and applications. *J Coat Technol Res* **19**(2), 377–402 (2022)
47. A. Sadoh, S. Hossain, N.M. Ravindra, Thermochromic polymeric films for applications in active intelligent packaging—an overview. *Micromachines* **12**(10) (2021)
48. G. Payne, Threads of evidence. *Chem Br* **38**(1), 37–39 (2002)
49. A. Abdollahi et al., Photoluminescent and chromic nanomaterials for Anticounterfeiting technologies: Recent advances and future challenges. *ACS Nano* **14**(11), 14417–14492 (2020)
50. A.M. Whaling, Material innovation: Thermochromatic inks. *J Appl Packag Res* **1**(1), 49–57 (2006)
51. T. Wu et al., A Thermochromic hydrogel for camouflage and soft display. *Adv Opt Mater* **8**(9), 2000031 (2020)
52. X. Gong et al., Thermochromic hydrogel-functionalized textiles for synchronous visual monitoring of on-demand in vitro drug release. *ACS Appl Mater Interfaces* **12**(46), 51225–51235 (2020)
53. J.D. LeSar et al., A novel Thermochromic liquid crystal fabric Design for the Early Detection of high-risk foot complications a proof-of-concept study. *J Am Podiatr Med Assoc* **107**(3), 200–207 (2017)
54. M. Bharara, J.E. Cobb, D.J. Claremont, Thermography and thermometry in the assessment of diabetic neuropathic foot: A case for furthering the role of thermal techniques. *Int J Low Extrem Wounds* **5**(4), 250–260 (2006)
55. S. Lakio, J. Heinamaki, J. Yliruusi, Colorful drying. *AAPS PharmSciTech* **11**(1), 46–53 (2010)
56. A.Q. Roy, M. Elham, Intelligent food packaging: Concepts and innovations. *Int J ChemTech Res* **9**(6), 669–676 (2016)
57. D.K. Nguyen et al., Synthesis and irreversible Thermochromic sensor applications of manganese violet. *Materials* **11**(9) (2018)
58. D.K. Nguyen, H. Lee, I.T. Kim, Synthesis and Thermochromic properties of Cr-doped Al₂O₃ for a reversible Thermochromic sensor. *Materials* **10**(5) (2017)
59. X.L. Luo et al., Reversible switching of the emission of Diphenyldibenzofulvenes by thermal and mechanical stimuli. *Adv Mater* **23**(29), 3261–+ (2011)
60. M.A. White, M. LeBlanc, Thermochromism in commercial products. *J Chem Educ* **76**(9), 1201–1205 (1999)
61. I. Butterworth et al., Exploiting thermochromic materials for the rapid quality assurance of physiotherapy ultrasound treatment heads. *Ultrasound Med Biol* **38**(5), 767–776 (2012)
62. T.Y. Yuan et al., Tunable Thermochromism of multifunctional charge-transfer-based supramolecular materials assembled in water. *Chem Mater* **29**(23), 9937–9945 (2017)
63. I.J. Kim, M. Ramalingam, Y.-A. Son, Investigation of reversible self-thermochromism in microencapsulated fluoran-based materials. *Dyes Pigments* **151**, 64–74 (2018)
64. D. Aitken et al., Textile applications of thermochromic systems. *Rev Prog Color Relat Top* **26**, 1–8 (1996)
65. P. Dai et al., Understanding the role of Electron donor in Truxene dye sensitized solar cells with cobalt electrolytes. *ACS Sustain Chem Eng* **5**(1), 97–104 (2017)
66. W. Zhang et al., A new approach for the preparation of durable and reversible color changing polyester fabrics using thermochromic leuco dye-loaded silica nanocapsules. *J Mater Chem C* **5**(32), 8169–8178 (2017)
67. I.J. Kim, R. Manivannan, Y.A. Son, Thermally reversible Fluorans: Synthesis, Thermochromic properties and real time application. *J Nanosci Nanotechnol* **18**(5), 3299–3305 (2018)
68. D.C. MacLaren, M.A. White, Competition between dye-developer and solvent-developer interactions in a reversible thermochromic system. *J Mater Chem* **13**(7), 1701–1704 (2003)
69. W. Oh et al., Synthesis of novel tert-butyl substituted fluorans and an investigation of their thermochromic behavior. *Dyes Pigments* **128**, 235–245 (2016)
70. S. Mehta et al., Fabrication of a reversible thermochromism based temperature sensor using an organic-inorganic composite system. *RSC Adv* **10**(36), 21270–21276 (2020)
71. K. Morigaki et al., Photopolymerization of diacetylene lipid bilayers and its application to the construction of micropatterned biomimetic membranes. *Langmuir* **18**(10), 4082–4089 (2002)
72. Y.T. Kim et al., Simultaneous evaluation of thermal and nonthermal effects of high intensity focused ultrasound on a tissue mimicking phantom. *Ultrasound Med Biol* **44**(8), 1799–1809 (2018)
73. A.S. Kavakli et al., Thermochromic nail polish as a novel indicator to predict infraclavicular brachial plexus block success a prospective cohort study. *Eur J Anaesthesiol* **36**(12), 911–917 (2019)
74. A.A. Dar, A.A. Ganie, Irreversible Thermochromism in organic salts of sulfonated Anils. *Cryst Growth Des* **20**(6), 3888–3897 (2020)
75. C.H. Lee et al., A polydiacetylene supramolecular system that displays reversible thermochromism. *Chem Lett* **36**(5), 682–683 (2007)
76. J.M. Kim et al., Rational design and in-situ FTIR analyses of colorimetrically reversible polydiacetylene supramolecules. *Macromolecules* **38**(22), 9366–9376 (2005)
77. A. Singh, R.B. Thompson, J.M. Schnur, Reversible Thermochromism in Photopolymerized phosphatidylcholine vesicles. *J Am Chem Soc* **108**(10), 2785–2787 (1986)
78. A. Perino et al., Self-assembled nanotubes and helical tapes from diacetylene nonionic amphiphiles. Structural studies before and after polymerization. *Langmuir* **27**(19), 12149–12155 (2011)
79. N. Abdullah et al., The basics and issues of Thermochromic liquid crystal calibrations. *Exp Thermal Fluid Sci* **34**(8), 1089–1121 (2010)
80. P.J. Collings, *Liquid Crystals: Nature's Delicate Phase of Matter, 2nd Edition* (Princeton University Press, 2002), p. 200
81. P. Collings, M. Hird, *An Introduction to Liquid Crystals: Chemistry and Physics* (Taylor & Francis, 1997)
82. M. Serebyuk et al., Room temperature operational thermochromic liquid crystals. *Chem Mater* **18**(10), 2513–2519 (2006)
83. E. Wagner, P. Stephan, Frequency response of a surface thermometer based on unencapsulated thermochromic liquid crystals. *Exp Thermal Fluid Sci* **31**(7), 687–699 (2007)
84. T. Kim, Surface heat transfer mapping using Thermochromic liquid crystal. Application of Thermo-Fluidic Measurement Techniques: an Introduction, 191–214 (2016)

85. V. Miskovic et al., Thermotropic liquid crystals for temperature mapping. *Front Bioeng Biotechnol* **10**, 806362 (2022)
86. S. Al Raisi et al., Renal artery branch denervation: Evaluation of lesion characteristics using a thermochromic liquid crystal phantom model. *Eur Heart J* **39**, 662–663 (2018)
87. Hallcrest Data Sheet Listing. "Handbook of Thermochromic Liquid Crystal Technology". [cited 2016 January 20. 2023]; Available from: http://www.hallcrest.com/downloads/randtk_TLC_Handbook.pdf
88. V.U. Kakade et al., Accurate heat transfer measurements using thermochromic liquid crystal. Part 1: Calibration and characteristics of crystals. *Int J Heat Fluid Flow* **30**(5), 939–949 (2009)
89. A. Mohammadabadi et al., Beam characterization of a custom, handheld focused ultrasound system using thermochromic liquid crystal films. *Medical Devices and Sensors* **4**(1) (2021)
90. C.K. McGarry et al., Tissue mimicking materials for imaging and therapy phantoms: A review. *Phys Med Biol* **65**(23) (2020)
91. S. Xu, H. Agarwal, M. Bernardo, R. Seifabadi, B. Turkbey, A. Partanen, A. Negussie, N. Glossop, P. Choyke, P. Pinto, B.J. Wood, *An MRI guided system for prostate laser ablation with treatment planning and multi-planar temperature monitoring* (SPIE, 2016), p. 9786
92. N. Pérez, K. Muffly, S.E. Saddow, Technical advance in silico and in vitro development of a new bipolar radiofrequency ablation device for renal denervation. *BMC Cardiovasc Disord* **21**(1) (2021)
93. Z. Miao et al., Thermochromic polyvinyl alcohol-iodine hydrogels with safe threshold temperature for infectious wound healing. *Advanced Healthcare Materials* **10**(18) (2021)
94. S. Dasgupta et al., Beam localization in HIFU temperature measurements using thermocouples, with application to cooling by large blood vessels. *Ultrasonics* **51**(2), 171–180 (2011)
95. S. Ambrogio et al., A polyvinyl alcohol-based Thermochromic material for ultrasound therapy phantoms. *Ultrasound Med Biol* **46**(11), 3135–3144 (2020)
96. A. Eranki et al., Boiling histotripsy lesion characterization on a clinical magnetic resonance imaging-guided high intensity focused ultrasound system. *PLoS one* **12**(3), e0173867 (2017)
97. L. Abdilla, C. Sammut, L.Z. Mangion, Dielectric properties of muscle and liver from 500 MHz–40 GHz. *Electromagnetic Biology and Medicine* **32**(2), 244–252 (2013)
98. V. Lopresto et al., Temperature dependence of thermal properties of ex vivo liver tissue up to ablative temperatures. *Phys Med Biol* **64**(10), 105016 (2019)
99. L. Bianchi et al., Thermophysical and mechanical properties of biological tissues as a function of temperature: A systematic literature review. *Int J Hyperth* **39**(1), 297–340 (2022)
100. E.C. Gregg, G.L. Palagallo, Acoustic impedance of tissue. *Investig Radiol* **4**(6), 357–363 (1969)
101. A.J. Duerinckx et al., Estimation of acoustic attenuation in liver using one megabyte of data and the zero-crossings technique. *Ultrasonics* **24**(6), 325–332 (1986)
102. P.R. Stauffer et al., Phantom and animal tissues for modelling the electrical properties of human liver. *Int J Hyperth* **19**(1), 89–101 (2003)
103. C.F. Chen et al., Clinical sound speed measurement in liver and spleen in vivo. *Ultrasound Imaging* **9**(4), 221–235 (1987)
104. U.L. Fahlenkamp et al., Correlation of native liver parenchyma T1 and T2 relaxation times and liver synthetic function tests: A pilot study. *Diagnostics* **11**(6), 1125 (2021)
105. S.I. Al Raisi et al., Renal artery branch denervation: Evaluation of lesion characteristics using a Thermochromic liquid crystal phantom model. *Heart Lung and Circulation* **29**(3), 445–451 (2020)
106. T. Thipayawat et al., in *41st Annual International Conference of the IEEE Engineering in Medicine and Biology Society (EMBC)*. Experimental Validation of the Multiphysics Modelling of Radiofrequency Ablation using Physical Phantom (Berlin, Germany, 2019)
107. P. Qian et al., A novel microwave catheter can perform noncontact circumferential endocardial ablation in a model of pulmonary vein isolation. *J Cardiovasc Electrophysiol* **26**(7), 799–804 (2015)
108. M. Eames et al., Low-cost Thermochromic quality assurance phantom for therapeutic ultrasound devices: A proof of concept. *Ultrasound Med Biol* **49**(1), 9 (2023)
109. K.K. Ng, R.T. Poon, Radiofrequency ablation for malignant liver tumor. *Surgical Oncology-Oxford* **14**(1), 41–52 (2005)
110. Z.P. Chai et al., An individually controlled multitined expandable electrode using active cannula-based shape morphing for on-demand conformal radiofrequency ablation lesions. *Advanced Intelligent Systems* **4**(7) (2022)
111. A.H.Y. Lau et al., Conformal devices for thermal sensing and heating in biomedical and human-machine interaction applications. *Advanced Intelligent Systems* **2**(4) (2020)
112. J.M. Lee et al., Multiple-electrode radiofrequency ablation of in vivo porcine liver: Comparative studies of consecutive monopolar, switching monopolar versus multipolar modes. *Investig Radiol* **42**(10), 676–683 (2007)
113. S. Woo et al., Small- and medium-sized hepatocellular carcinomas: Monopolar radiofrequency ablation with a multiple-electrode switching system—mid-term results. *Radiology* **268**(2), 589–600 (2013)
114. J.H. Yoon et al., Monopolar radiofrequency ablation using a dual-switching system and a separable clustered electrode: Evaluation of the in vivo efficiency. *Korean J Radiol* **15**(2), 235–244 (2014)
115. K. Han et al., A single-center retrospective analysis of Periprocedural variables affecting local tumor progression after radiofrequency ablation of colorectal Cancer liver metastases. *Radiology* **298**(1), 212–218 (2021)
116. J.T. Loh et al., Efficacy of needle-placement technique in radiofrequency ablation for treatment of lumbar facet arthropathy. *J Pain Res* **8**, 687–694 (2015)
117. M.H. Chen et al., Treatment efficacy of radiofrequency ablation of 338 patients with hepatic malignant tumor and the relevant complications. *World J Gastroenterol* **11**(40), 6395–6401 (2005)
118. G. Antoch et al., Value of CT volume imaging for optimal placement of radiofrequency ablation probes in liver lesions. *J Vasc Interv Radiol* **13**(11), 1155–1161 (2002)
119. E. Sjolie et al., 3D ultrasound-based navigation for radiofrequency thermal ablation in the treatment of liver malignancies. *Surg Endosc Other Interv Tech* **17**(6), 933–938 (2003)
120. M.B. Sano, M.R. DeWitt, Thermochromic tissue phantoms for evaluating temperature distribution in simulated clinical applications of pulsed electric field therapies. *Bioelectricity* **2**(4), 362–371 (2020)
121. A. Dabbagh et al., Reusable heat-sensitive phantom for precise estimation of thermal profile in hyperthermia application. *Int J Hyperth* **30**(1), 66–74 (2014)
122. J.W. Karanian et al., Monopolar radiofrequency energy delivered by a conductive endovascular basket or guidewire leads to thermal occlusion in a swine model. *J Vasc Interv Radiol* **31**(11), 1874–1885 (2020)
123. M.J. Rivera et al., Analytical validation of COMSOL multiphysics for theoretical models of radiofrequency ablation including the hyperbolic bioheat transfer equation. *Annu Int Conf IEEE Eng Med Biol Soc* **2010**, 3214–3217 (2010)
124. I.A. Chang, U.D. Nguyen, Thermal modeling of lesion growth with radiofrequency ablation devices. *Biomed Eng Online* **3** (2004)
125. K. Segura Félix et al., Computational FEM model and phantom validation of microwave ablation for segmental microcalcifications in breasts using a coaxial double-slot antenna. *Biomed Res Int* **2021**, 1–10 (2021)
126. M. Trujillo, E. Berjano, Review of the mathematical functions used to model the temperature dependence of electrical and thermal conductivities of biological tissue in radiofrequency ablation. *Int J Hyperth* **29**(6), 590–597 (2013)
127. Z. Liu et al., Characterization of the RF ablation-induced 'oven effect': The importance of background tissue thermal conductivity on tissue heating. *Int J Hyperth* **22**(4), 327–342 (2006)
128. T. Nolte et al., Study of flow effects on temperature-controlled radiofrequency ablation using phantom experiments and forward simulations. *Med Phys* **48**(9), 4754–4768 (2021)
129. T. Boers et al., Matrix 3D ultrasound-assisted thyroid nodule volume estimation and radiofrequency ablation: A phantom study. *European Radiology Experimental* **5**(1) (2021)
130. W.W.B. Chik et al., High spatial resolution thermal mapping of radiofrequency ablation lesions using a novel thermochromic liquid crystal myocardial phantom. *J Cardiovasc Electrophysiol* **24**(11), 1278–1286 (2013)
131. D. Prochnau et al., Renal denervation with standard radiofrequency ablation catheter is effective in 24-hour ambulatory blood pressure

- reduction follow-up at 1/3/6/12 months. *Neth Hear J* **24**(7-8), 449–455 (2016)
132. S.I. Al Raisi et al., Comparison of new-generation renal artery denervation systems: Assessing lesion size and thermodynamics using a thermochromic liquid crystal phantom model. *Eurointervention* **13**(10), 1242–1247 (2017)
 133. D.T. Nguyen et al., Effect of radiofrequency energy delivery in proximity to metallic medical device components. *Heart Rhythm* **12**(10), 2162–2169 (2015)
 134. K.-H. Kuck et al., A novel radiofrequency ablation catheter using contact force sensing: Toccata study. *Heart Rhythm* **9**(1), 18–23 (2012)
 135. W.W.B. Chik et al., Intracranial nonthermal irreversible ablations with duty cycle power delivery negate effects of ablation catheter motion. *Circ Arrhythm Electrophysiol* **7**(5), 920–928 (2014)
 136. T. Thipayawat et al., Experimental validation of the multiphysics modelling of radiofrequency ablation using physical phantom. *Annu Int Conf IEEE Eng Med Biol Soc* **2019**, 154–157 (2019)
 137. R.V. Davalos, I.L.M. Mir, B. Rubinsky, Tissue ablation with irreversible electroporation. *Ann Biomed Eng* **33**(2), 223–231 (2005)
 138. P.A. Garcia et al., Intracranial nonthermal irreversible electroporation: In Vivo Analysis. *J Membr Biol* **236**(1), 127–136 (2010)
 139. M.J. van Gemert et al., Irreversible electroporation: Just another form of thermal therapy? *Prostate* **75**(3), 332–335 (2015)
 140. K.F. Chu, D.E. Dupuy, Thermal ablation of tumours: Biological mechanisms and advances in therapy. *Nat Rev Cancer* **14**(3), 199–208 (2014)
 141. B. Al-Sakere et al., Tumor ablation with irreversible electroporation. *PLoS One* **2**(11) (2007)
 142. H. Shafiee, P.A. Garcia, R.V. Davalos, A preliminary study to delineate irreversible electroporation from thermal damage using the arrhenius equation. *J Biomech Eng* **131**(7), 074509 (2009)
 143. P.F. Laeseke et al., Multiple-antenna microwave ablation: Spatially distributing power improves thermal profiles and reduces invasiveness. *J Interv Oncol* **2**(2), 65–72 (2009)
 144. C.M. Harari et al., Microwave ablation: Comparison of simultaneous and sequential activation of multiple antennas in liver model systems. *Radiology* **278**(1), 95–103 (2016)
 145. E.M. Knavel et al., High-powered gas-cooled microwave ablation: Shaft cooling creates an effective stick function without altering the ablation zone. *AJR Am J Roentgenol* **198**(3), W260–W265 (2012)
 146. L.S. Poulou et al., Percutaneous microwave ablation vs radiofrequency ablation in the treatment of hepatocellular carcinoma. *World J Hepatol* **7**(8), 1054–1063 (2015)
 147. O. Seror et al., Radiofrequency ablation with internally cooled versus perfused electrodes for the treatment of small hepatocellular carcinoma in patients with cirrhosis. *J Vasc Interv Radiol* **19**(5), 718–724 (2008)
 148. M.H.H. Tehrani et al., Use of microwave ablation for thermal treatment of solid tumors with different shapes and sizes—a computational approach. *PLoS One* **15**(6), e0233219 (2020)
 149. W.C. Dewey, Arrhenius relationships from the molecule and cell to the clinic. *Int J Hyperth* **10**(4), 457–483 (1994)
 150. M.H.H. Tehrani et al., Use of microwave ablation for thermal treatment of solid tumors with different shapes and sizes—a computational approach. *PLoS One* **15**(6) (2020)
 151. Y. Zhou et al., A thermochromic tissue-mimicking phantom model for verification of ablation plans in thermal ablation. *Ann Transl Med* **9**(4), 354 (2021)
 152. Z. Starek et al., Efficacy and safety of novel temperature-controlled radiofrequency ablation system during pulmonary vein isolation in patients with paroxysmal atrial fibrillation: TRAC-AF study. *J Interv Card Electrophysiol* **64**(2), 375–381 (2022)
 153. C.M. Pacella et al., Percutaneous laser ablation in the treatment of hepatocellular carcinoma with small tumors: Analysis of factors affecting the achievement of tumor necrosis. *J Vasc Interv Radiol* **16**(11), 1447–1457 (2005)
 154. M. De Landro et al., Fiber Bragg grating sensors for performance evaluation of fast magnetic resonance thermometry on synthetic phantom. *Sensors* **20**(22), 6468 (2020)
 155. E. Knull et al., Toward mechatronic MRI-guided focal laser ablation of the prostate: Robust registration for improved needle delivery. *Med Phys* **50**(3), 1259–1273 (2023)
 156. Y. Chen et al., MRI-guided robotically assisted focal laser ablation of the prostate using canine cadavers. *IEEE Trans Biomed Eng* **65**(7), 1434–1442 (2018)
 157. E. Knull et al., Design and validation of an MRI-compatible mechatronic system for needle delivery to localized prostate cancer. *Med Phys* **48**(9), 5283–5299 (2021)
 158. S. Xu et al., *An MRI guided system for prostate laser ablation with treatment planning and multi-planar temperature monitoring*. in *Conference on SPIE Image-Guided Procedures, Robotic Interventions, and Modeling* (San Diego, CA, 2016)
 159. R. Seifabadi et al., *MRI robot for prostate focal laser ablation: An ex vivo study in human prostate*. *Journal of Imaging* **4**(12) (2018)
 160. A. Clark et al., Microbubble-enhanced heating: Exploring the effect of microbubble concentration and pressure amplitude on high-intensity focused ultrasound treatments. *Ultrasound Med Biol* **47**(8), 2296–2309 (2021)
 161. M. Sadeghi-Goughari, S. Jeon, H.-J. Kwon, Analytical and numerical model of high intensity focused ultrasound enhanced with nanoparticles. *IEEE Trans Biomed Eng* **67**(11), 3083–3093 (2020)
 162. P. Rischmann et al., Focal high intensity focused ultrasound of unilateral localized prostate Cancer: A prospective multicentric Hemiablation study of 111 patients. *Eur Urol* **71**(2), 267–273 (2017)
 163. R. Bass et al., Oncologic and functional outcomes of partial gland ablation with high intensity focused ultrasound for localized prostate Cancer. *J Urol* **201**(1), 113–119 (2019)
 164. M.C.L. Peek et al., High-intensity focused ultrasound in the treatment of breast fibroadenomata (HIFU-F trial). *Int J Hyperth* **34**(7), 1002–1009 (2018)
 165. L.M. Guan, G. Xu, Damage effect of high-intensity focused ultrasound on breast cancer tissues and their vascularities. *World Journal of Surgical Oncology* **14** (2016)
 166. M. Marinova, T. Wilhelm-Buchstab, H. Strunk, Advanced pancreatic Cancer: High-intensity focused ultrasound (HIFU) and other local ablative therapies. *Rofo-Fortschritte Auf Dem Gebiet Der Rontgenstrahlen Und Der Bildgebenden Verfahren* **191**(3), 216–227 (2019)
 167. A.S. Sehmbi et al., Systematic review of the role of high intensity focused ultrasound (HIFU) in treating malignant lesions of the hepatobiliary system. *HPB (Oxford)* **23**(2), 187–196 (2021)
 168. G. ter Haar, HIFU tissue ablation: Concept and devices. *Adv Exp Med Biol* **880**, 3–20 (2016)
 169. E. Maloney, J.H. Hwang, Emerging HIFU applications in cancer therapy. *Int J Hyperth* **31**(3), 302–309 (2015)
 170. R. Cirincione et al., High-intensity focused ultrasound-and radiation therapy-induced Immuno-modulation: Comparison and potential opportunities. *Ultrasound Med Biol* **43**(2), 398–411 (2017)
 171. X.R. Zhang et al., Focused ultrasound radiosensitizes human cancer cells by enhancement of DNA damage. *Strahlenther Onkol* **197**(8), 730–743 (2021)
 172. J. Huang et al., Experimental validation of a tractable numerical model for focused ultrasound heating in flow-through tissue phantoms. *J Acoust Soc Am* **116**(4), 2451–2458 (2004)
 173. P.T.S. Borman et al., Towards real-time thermometry using simultaneous multislice MRI. *Phys Med Biol* **61**(17), N461–N477 (2016)
 174. M.O. Kohler et al., in *8th International Symposium on Therapeutic Ultras*. Volumetric HIFU Ablation guided by Multiplane MRI Thermometry (Minneapolis, MN, 2008)
 175. M. Marx, K.B. Pauly, Improved MRI thermometry with multiple-Echo spirals. *Magn Reson Med* **76**(3), 747–756 (2016)
 176. B. Quesson et al., Real-time volumetric MRI thermometry of focused ultrasound ablation in vivo: A feasibility study in pig liver and kidney. *NMR Biomed* **24**(2), 145–153 (2011)
 177. L. Fura, T. Kujawska, Selection of exposure parameters for a HIFU ablation system using an Array of thermocouples and numerical simulations. *Archives of Acoustics* **44**(2), 349–355 (2019)
 178. B. Karaboce et al., in *12th IEEE International Symposium on Medical Measurements and Applications (MeMeA)*. Experimental Investigations of Viscous Heating Effect of Thermocouples under Focused Ultrasound Applications (Rochester, MN, 2017)
 179. A.L.M. Gerardo, A.V.O. Gerardo, in *New Developments in Liquid Crystals. Three Dimensional Temperature Distribution Analysis of Ultrasound*

- Therapy Equipments Using Thermochromic Liquid Crystal Film* (I-Tech, Vienna, Austria, 2009), p. 234
180. A.M. Ivory et al., *Development and testing of a system for controlled ultrasound hyperthermia treatment with a phantom device* (IEEE trans Ultrason Ferroelectr Freq control, 2023)
 181. M. Eames et al., *Low-COST THERMOCHROMIC quality assurance phantom for therapeutic ultrasound devices: A proof of concept*. *Ultrasound Med Biol* **49**(1), 269–277 (2023)
 182. C. Lafon et al., *Gel phantom for use in high-intensity focused ultrasound dosimetry*. *Ultrasound Med Biol* **31**(10), 1383–1389 (2005)
 183. P.M. Edwards, *Neurotoxicity of acrylamide and its analogs and effects of these analogs and other agents on acrylamide neuropathy*. *Br J Ind Med* **32**(1), 31 (1975)
 184. H.T.M. Phan et al., *Investigation of bovine serum albumin (BSA) attachment onto self-assembled monolayers (SAMs) using combinatorial quartz crystal microbalance with dissipation (QCM-D) and spectroscopic ellipsometry (SE)*. *PLoS One* **10**(10), e0141282/1–e0141282/20 (2015)
 185. N.P. Brodin et al., *A simple method for determining the coagulation threshold temperature of transparent tissue-mimicking thermal therapy gel phantoms: Validated by magnetic resonance imaging thermometry*. *Med Phys* **43**(3), 1167–1174 (2016)
 186. M. McDonald et al., *Multi-modality tissue-mimicking phantom for thermal therapy*. *Phys Med Biol* **49**, 2767–2778 (2004)
 187. T. Iwahashi et al., *Visualization of temperature distribution around focal area and near fields of high intensity focused ultrasound using a 3D measurement system*. *Advanced Biomedical Engineering* **7**, 1–7 (2018)
 188. R. Takagi et al., *A visualization method for a wide range of rising temperature induced by high-intensity focused ultrasound using a tissue-mimicking phantom*. *Int J Hyperth* **39**(1), 22–33 (2022)
 189. G. Menikou et al., *MRI-compatible breast/rib phantom for evaluating ultrasonic thermal exposures*. *Int J Med Robot* **14**(1) (2018)
 190. W. Zhang et al., *Anatomic thermochromic tissue-mimicking phantom of the lumbar spine for pre-clinical evaluation of MR-guided focused ultrasound (MRgFUS) ablation of the facet joint*. *Int J Hyperth* **38**(1), 130–135 (2021)
 191. L. Morchi et al., *A reusable Thermochromic phantom for testing high intensity focused ultrasound technologies*. *Annual international conference of the IEEE engineering in medicine and biology society. IEEE engineering in medicine and biology society Annual International Conference* **2021**, 1431–1434 (2021)
 192. J. Kim, M. Kim, *Focal position control of ultrasonic transducer made of Plano-concave form piezoelectric vibrator*. *Ultrasonics* **121** (2022)
 193. K.R. Navarra et al., *The application of pressure- and temperature-sensitive paints to an advanced compressor*. *Journal of Turbomachinery-Transactions of the Asme* **123**(4), 823–829 (2001)
 194. M. Zubair, R. Dickinson, *Calculating the effect of ribs on the focus quality of a therapeutic spherical random phased Array*. *Sensors* **21**(4) (2021)
 195. N. Farr et al., *Tissue-mimicking thermochromic rib phantom for characterization of intercostal HIFU sonications and beam-shaping methods*. *Journal of therapeutic. Ultrasound* **4**(1) (2016)
 196. N. Farr et al., *Development of a tissue-mimicking rib phantom for MR-HIFU therapy*. *Journal of Therapeutic Ultrasound* **5**, 89–90 (2016)
 197. D. Kim, J.P. Erinjeri, *Postablation immune microenvironment: Synergy between interventional oncology and Immuno-oncology*. *Semin Interv Radiol* **36**(4), 334–342 (2019)
 198. M. Payne, S.H. Bossmann, M.T. Basel, *Direct treatment versus indirect: Thermo-ablative and mild hyperthermia effects*. *Wiley Interdiscip Rev Nanomed Nanobiotechnol* **12**(5), e1638 (2020)
 199. N.D. Sheybani et al., *Focused ultrasound hyperthermia augments release of glioma-derived extracellular vesicles with differential immunomodulatory capacity*. *Theranostics* **10**(16), 7436–7447 (2020)
 200. R. Slovak et al., *Immuno-thermal ablations - boosting the anticancer immune response*. *J Immunother Cancer* **5**(1), 78 (2017)
 201. S. Shen et al., *Screening for immune-potentiating antigens from hepatocellular carcinoma patients after radiofrequency ablation by serum proteomic analysis*. *BMC Cancer* **18**, 117/1–117/8 (2018)
 202. R.J.E. Van Den Bijgaart et al., *Immune modulation plus tumor ablation: Adjuvants and antibodies to prime and boost anti-tumor immunity in situ*. *Front Immunol* **12**, 617365 (2021)
 203. C. Rossmanna, D. Haemmerich, *Review of temperature dependence of thermal properties, dielectric properties, and perfusion of biological tissues at hyperthermic and ablation temperatures*. *Crit Rev Biomed Eng* **42**(6), 467–492 (2014)
 204. D. Jaque et al., *Nanoparticles for photothermal therapies*. *Nanoscale* **6**(16), 9494–9530 (2014)
 205. S.N. Goldberg et al., *Percutaneous radiofrequency tissue ablation: Optimization of pulsed-radiofrequency technique to increase coagulation necrosis*. *J Vasc Interv Radiol* **10**(7), 907–916 (1999)
 206. M. Friedman et al., *Radiofrequency ablation of cancer*. *Cardiovasc Intervent Radiol* **27**(5), 427–434 (2004)

Publisher's Note

Springer Nature remains neutral with regard to jurisdictional claims in published maps and institutional affiliations.